Research Highlights

Ambipolar Nickel Dithiolene Complex Semiconductors: from One to Two-Dimensional Electronic Structures Based upon Alkoxy Chain Lengths

Mori and Ozaki Groups

Molecular semiconductors, which are mainly based on π-conjugated organic molecules are crucial materials in fundamental research and electronics because they are flexible, light-weight, and can be solution-processed in a cost-effective, energy-saving manner. Among them, materials that can transport both holes and electrons are required for next-generation devices, such as organic light-emitting transistors and organic solar cells. Hence, materials that physically combine hole- and electron-transporting semiconductors in mixed or bi-layered forms have been used as dual transporters. However, poor interfacial contact between the two materials, where charge recombination or separation occurs, often leads to poor quantum efficiencies and reproducibilities. Instead, single-component ambipolar semiconductors that can transport both holes and electrons are promising materials capable of overcoming these obstacles. Polymer-based materials, such as donor–acceptor copolymers, exhibited ambipolar semiconducting characteristics. However, the structural inhomogeneity based on the inevitable wide-ranged molecular weight distribution severely hampered access to the structural insights and the conduction mechanism, hampering the establishment of the materials designing guidelines. Therefore, we focused on the single-molecular-weight ambipolar organic semiconductors that offer excellent tunability of electronic structures and crystallinity to access the structural insights and conduction mechanism.

Our groups have designed and synthesized d/π-conjugated molecules, Ni(4OR) [R = Me, Et, Pr] (Fig. 1) [1,3], in which the nickel element with d electrons plays a central role. These molecules are highly stable and do not react easily with water or oxygen, and are also attractive because they can be easily synthesized using nickel, which is a relatively inexpensive metallic material. In addition to the electronic structure and properties, molecular semiconductors with excellent carrier transport properties requires seemingly contradictory properties: high crystallinity to enable highly ordered and highly dimensional stacking states, and high solubility to realize excellent thin-film processability. The research group searched for new materials that fulfil these conditions among combinations of d/π-conjugated backbone and side chains, and found a group of d/π-conjugated molecules that achieve both.

Unexpectedly, it was found that slight differences in the number of carbons on the side chains dramatically changed the stacking structure in single crystals. Those with one carbon substituent exhibited a one-dimensional stacking pattern, while those with two or three carbons exhibited a herringbone-type stacking pattern with a two-dimensional electronic structure, which is advantageous for stable device operation (Fig. 1). The latter stacking pattern was reproduced in thin films with a thickness of several tens of nanometres, which were constructed by solution coating, and highly ordered crystalline thin films were successfully realized. Field-effect transistor devices in which the resulting thin films were inserted as semiconductor layers exhibited ambipolar charge transport properties and showed high levels of both carrier mobility (up to 10^{-2} $cm^2V^{-1}s^{-1}$) and on-off ratio (10^5). These performances were demonstrated in an open environment without the strict exclusion of water and oxygen, enabling the realization of a new ambipolar semiconductors with high stability, solution-dispensable and high mobility.

In summary, novel molecular ambipolar semiconductors, Ni(4OR) [R = Me, Et, Pr], which are inexpensive and easy to synthesize, resistant to reaction with water and oxygen, and possible to solution process, have been developed and exhibited excellent carrier mobility and on-off ratio. The availability of structural information at the atomic level has enabled detailed electronic structure and conduction mechanism analysis, and has revealed molecular design guidelines for superior semiconductors, which have not been established for polymer materials. In the future, it is

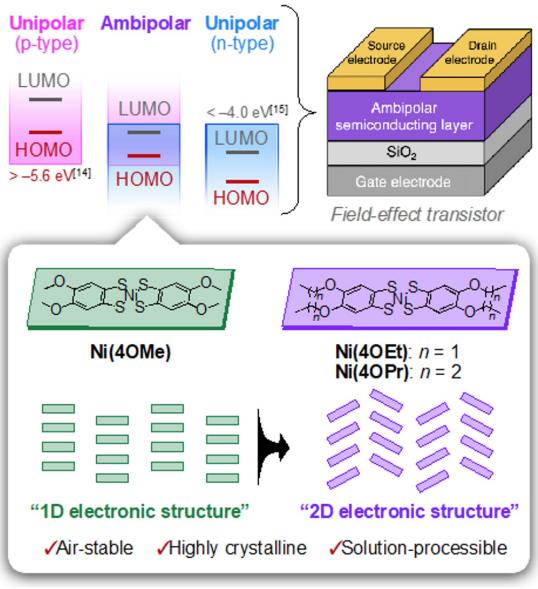

Fig. 1. (Top) Electronic structure requirements for ambipolar semiconductors used in field-effect transistors (FET), where the electronic structure requirements imposed on p-type/n-type semiconductors must be compatible with each other. (Bottom) Schematic diagram of the structural formula of the novel complex developed in this study and its molecular stacking pattern. Single crystal X-ray structure analysis revealed a dramatic modulation of the molecular stacking pattern associated with a slight extension of the side chains, and theoretical calculations confirmed the acquisition of dimensionality (D) from 1D to 2D.

expected that d/π-conjugated molecules will be developed by utilizing the high degree of structural freedom based on the combination of the central metal and ligand towards high transport properties through a higher-dimensional electronic structure based on changes in stacking pattern according to the number of carbons on the side chains. Such a detailed material design strategy using molecular materials can be extended not only to electrically conductive materials but also to various applications such as magnetic materials and photo-functional materials and is expected to make a significant contribution to the development of next-generation organic electronic devices.

References

[1] M. Ito, T. Fujino, L. Zhang, S. Yokomori, T. Higashino, R. Makiura, K. J. Takeno, T. Ozaki, and H. Mori, J. Am. Chem. Soc. **145**, 2127 (2023).

[2] D. Zhang, S. Yokomori, R. Kameyama, C. Zhao, A. Ueda, L. Zhang, R. Kumai, Y. Murakami, H. Meng, and H. Mori, ACS Appl. Mater. Interfaces **13**, 989 (2021).

[3] S. Yokomori, S. Dekura, A. Ueda, R. Kumai, Y. Murakami, and H. Mori, J. Mater. Chem. **9**, 10718 (2019).

Authors

M. Ito, T. Fujino, L. Zhang, S. Yokomori, T. Higashino, R. Makiura, K. J. Takeno, T. Ozaki, and H. Mori

Quantized Thermoelectric Hall Effects in Nodal-Line Semimetals at the High-Magnetic-Field Quantum Limit

Osada Group

The "quantized thermoelectric Hall effect (QTHE)" has been established theoretically and experimentally in 3D Dirac/Weyl semimetals with nodal points, at the high-magnetic-field quantum limit (QL). Reflecting their characteristic N = 0 chiral Landau subband (Fig. 1(a)), their thermoelectric Hall conductivity α_{xy} takes a constant value (Fig. 1(b)), which is independent of magnetic field and carrier number, resulting in the boundless linear increase of the Seebeck coefficient $S_{xx} \sim \alpha_{xy} / \sigma_{xy}$. This feature brings about high-performance thermoelectricity. The more remarkable QTHE was proposed in the 2D massless Dirac fermion system with nodal points at the QL. In this case, α_{xy} takes a quantized constant value of $(4 \log 2)\, k_B\, e / h$, which is independent of temperature, magnetic field, and carrier density, so that the boundless increase of S_{xx} can be expected even at low temperatures. Here, we have theoretically and experimentally investigated the possible QTHE in the 3D topological semimetals with straight nodal lines at the QL.

First, we exhibited that the QTHE can more generally appear even in a part of the 3D nodal-line semimetals in addition to the nodal-point semimetals [1]. We considered the 3D semimetals with straight parallel nodal lines. For example, they can be realized as multilayer systems where 2D massless Dirac fermion layers stack with weak interlayer coupling. When the magnetic field is applied parallel to the straight nodal lines, the N = 0 ground Landau subband (Fig. 1(c)), which consists of the N = 0 Landau level of each 2D layer, plays the similar role as the pair of the N = 0 chiral Landau subbands in Dirac/Weyl semimetals, and also causes the similar QTHE (Fig. 1(d)). The constant value of α_{xy} contains the dispersion parameter, and it is proportional to temperature but independent of carrier density.

We quantitatively discussed the possible QTHE in graphite as an example of the nodal-line semimetal [1]. In 3D graphite, the conduction and valence bands quadratically touch along the H-K-H edge of the Brillouin zone, forming nodal lines. Based on the Landau subband configuration obtained from the Slonczewski-Weiss-McClure model (Fig. 1(e)), we calculated α_{xy} as a function of magnetic field and confirmed the QTHE plateau formation with the value $\alpha_{xy}^{(\mathrm{sheet})} \sim 0.036\ [\mathrm{K}^{-1}]\ T\ (k_B\, e / h)$ per bilayer at the quasi-QL $|B_z| > 8$ T, where only two ground subbands (N' = -1, 0) locate at the Fermi level (Fig. 1(f)).

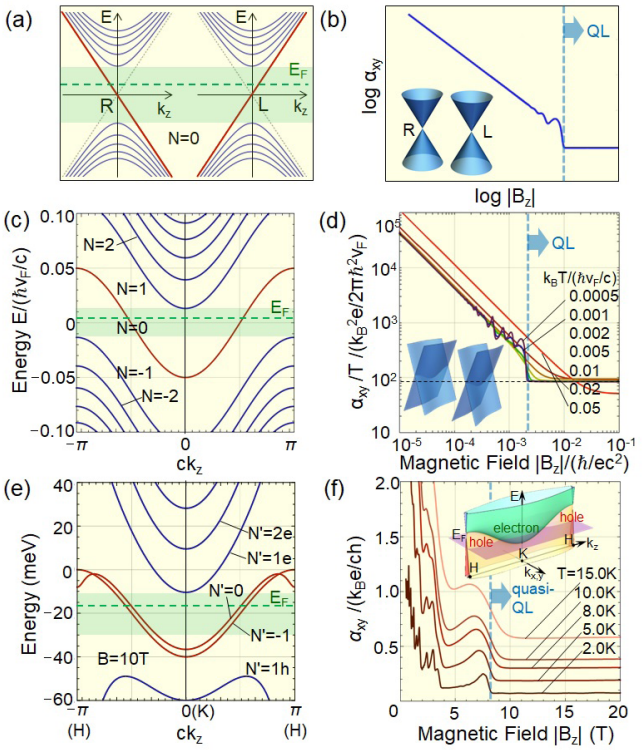

Fig. 1. Landau subband configuration and thermoelectric Hall conductivity α_{xy} in (a)(b) Dirac/Weyl semimetals, (c)(d) straight nodal-line semimetals, and (e)(f) graphite. The plateau due to the QTHE appears in the QL region [1].

Next, we performed the thermoelectric measurement on graphite to confirm the QTHE [2]. The resistivity (ρ_{xx}, ρ_{xy}) and thermopower (S_{xx}, S_{xy}) were measured simultaneously to compute α_{xy}. We could successfully obtain the plateau of α_{xy} at the quasi-QL (Fig. 2), which quantitatively agrees with our calculation. In graphite, the Hall conductivity σ_{xy} is not simply proportional to $1/B$ but shows complicated B-dependence, so that the boundless increase of S_{xx} cannot be observed.

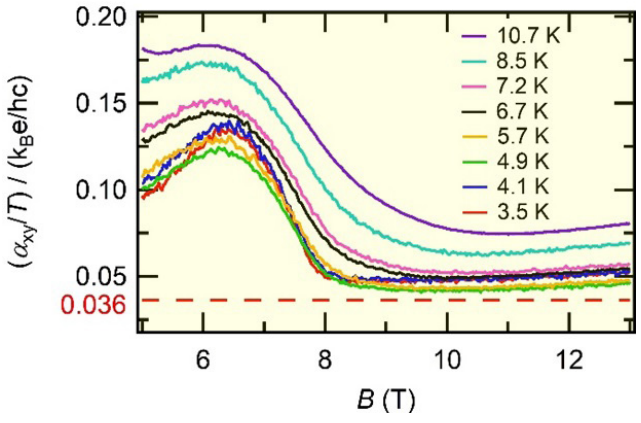

Fig. 2. Thermoelectric Hall conductivity α_{xy} measured in bulk graphite. The QTHE plateau corresponding to the calculation (Fig. 1(f)) can be seen above 8 T [2].

In addition, we theoretically investigated the quantum size effect on the QTHE in thin-film graphite [1]. When the thickness of graphite is decreased, the Landau subbands is discretized into many levels by the quantization of the inter-layer wave number. This causes the dimensional crossover of the QTHE from 3D to 2D.

References

[1] T. Osada, T. Ochi, and T. Taen, J. Phys. Soc. Jpn. **91**, 063701 (2022).

[2] A. Kiswandhi, T. Ochi, T. Taen, M. Sato, K. Uchida, and T. Osada, Phys. Rev. B **107**, 195106 (2023).

Authors

T. Osada, A. Kiswandhi, T. Ochi, M. Sato, K. Uchida, and T. Taen

Topological Thermal Hall Effect of Magnons in Magnetic Skyrmion Lattice

Yamashita Group

Currently, research on the effects of emergent magnetic fields created by spin structures in solids is attracting much attention. This is because such emergent magnetic fields directly affect the wave function of electrons, giving rise to more drastic effects on electrons than those caused by an external magnetic field. One of the most celebrated examples is the emergent magnetic field produced by a magnetic skyrmion – a vortex texture of spins in a magnetic solid (see Fig. 1(a)). For conduction electrons in a metal, it is well known that the topological Hall effect is given by the emergent magnetic field of the magnetic skyrmions of which the field strength is equivalent to several hundred tesla in external magnetic field. On the other hand, it has been unknown how the emergent field acts on charge-neutral heat carriers in insulators, such as magnons and phonons.

In this study [1], we investigated in detail the thermal transport properties in GaV_4Se_8, a ferromagnetic insulator in which a magnetic cycloidal phase at zero-field below the Curie temperature is transformed into a magnetic skyrmion phase by applying a magnetic field (Fig. 1(c)). We find that, whereas the thermal Hall effect is absent both in the cycloidal and the forced-ferromagnetic phases, a clear thermal Hall effect appears in the magnetic skyrmion phase (Fig. 1(b)). A color plot of the thermal Hall conductivity (κ_{xy}) demonstrates the position of the magnetic skyrmion phase in the B–T phase diagram as shown in Fig. 1(c). In addition, the thermal Hall signal is increased by increasing the domain volume of the magnetic skyrmion phase by cooling the sample under a magnetic field through the structural phase transition. These results indicate that the observed thermal Hall signal is caused by the emergent magnetic field of the magnetic skyrmion lattice.

We confirm that this is indeed the case by theoretically calculating the heat transport of the magnons in the magnetic skyrmion lattice. We find that the calculated magnon bands, which are folded by the lattice of the magnetic skyrmions, acquire non-trivial Chern number. In particular, as shown by the Fig. 2(a), the magnon bands around the top of the lowest

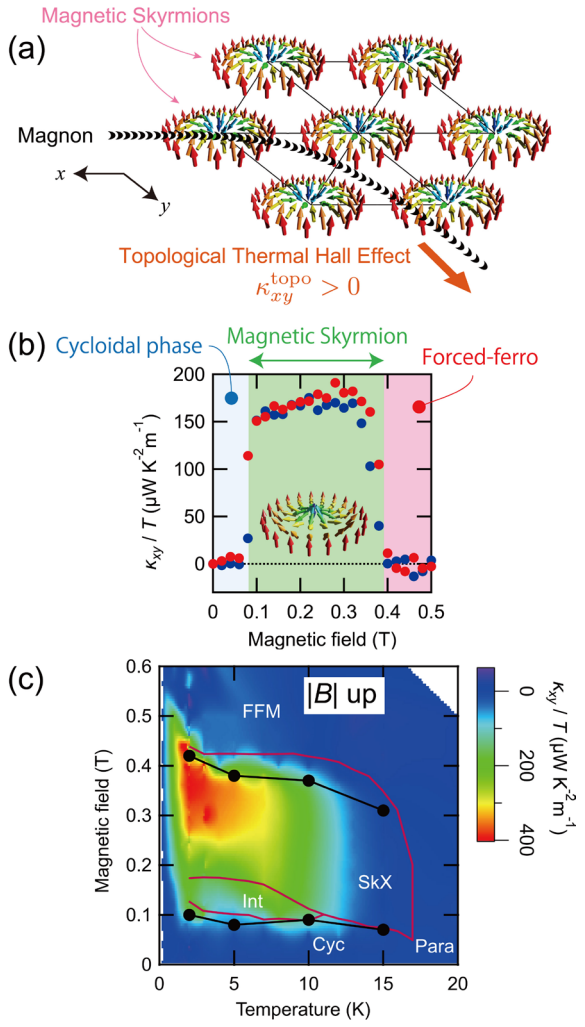

Fig. 1. (a) A schematic illustration of the topological thermal Hall effect of magnons in the lattice of magnetic skyrmions. The flow of the magnons is bent by the emergent magnetic field produced by the vortex spin texture of the magnetic skyrmions. (b) The magnetic field dependence of the thermal Hall conductivity (κ_{xy}). A finite κ_{xy} sharply appears in the magnetic skyrmion phase (green shared area), but disappears in the cycloidal (blue) and the forced-ferromagnetic (pink) phases. (c) A color plot of κ_{xy}/T observed in the magnetization process ("|B| up").

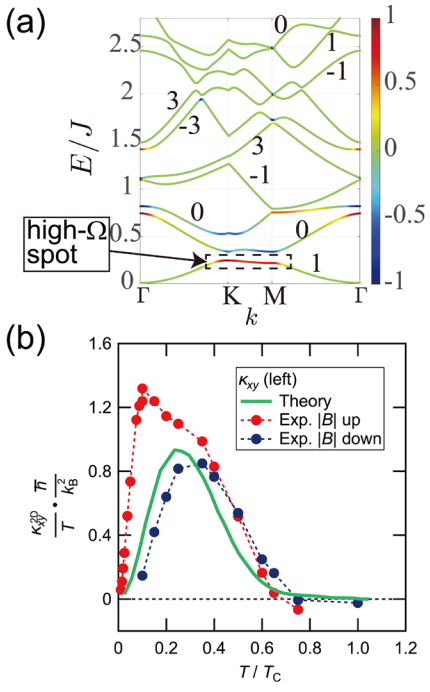

Fig. 2. (a) Energy bands of the magnons in the lattice of magnetic skyrmions along high-symmetry points. Color denotes the Berry curvature that is normalized in each band. (b) Temperature dependence of κ_{xy}/T by calculation (solid line) and experiments (symbols). Experimental data obtained at 0.36 T in the magnetizing (|B| up) and 0.2 T in the demagnetizing (|B| down) processes are shown in red and blue circles, respectively. To fit with the theoretical result, the horizontal axis of the experimental data is normalized by the Curie temperature T_C = 20 K. See [1] for more details.

magnon band have a large Berry curvature ("high-Ω spot" in Fig. 2(a)), giving rise to the topological thermal Hall effect of the magnons. Based on this magnon band calculation, we estimate the temperature dependence of κ_{xy}, and find that our calculation well reproduces the experimental result observed in the demagnetization process (see the green solid line and the blue data in Fig. 2(b)). On the other hand, κ_{xy} observed in the magnetization process shows a very different temperature dependence that persists at lower temperature than κ_{xy} in the demagnetization process (red data in Fig. 2(b)). This unexpected hysteresis might indicate that the lattice of the magnetic skyrmion is more disordered in the magnetization process, suggesting a difference in the skyrmion lattice depending on whether it is formed from the forced-ferromagnetic phase or the cycloidal phase. Although this possibility should be scrutinized by future measurements of the skyrmion lattice, this hysteresis in κ_{xy} shows a high sensitivity of the thermal Hall measurements for the skyrmion lattice structure not attainable by other measurements.

Reference
[1] M. Akazawa, H.-Y. Lee, H. Takeda, Y. Fujima, Y. Tokunaga, T. Arima, J. H. Han, and M. Yamashita, Phys. Rev. Research **4**, 043085 (2022).

Authors
M. Akazawa, H.-Y. Lee[a], H. Takeda, Y. Fujima[b], Y. Tokunaga[b], T. Arima[b], J. H. Han[c], and M. Yamashita
[a]Korea University
[b]University of Tokyo
[c]Sungkyunkwan University

Enhanced Bulk Photovoltaic Effect in Strained 3R-MoS_2

Ideue Group

Bulk photovoltaic effect, which indicates the generation of spontaneous photocurrent in uniform materials instead of conventional p-n junctions, is attracting considerable interest due to its microscopic origins related to the electronic band topology or geometry as well as its potential to achieve a high solar energy conversion efficiency. So far, bulk photovoltaic effect has been reported in a variety of noncentrosymmetric quantum materials and several strategies to enhance the photocurrent magnitude are also developed. Among them, strain application is a simple method for controlling the crystal structures or electronic states and thus an effective way for realizing the enhanced photovoltaic signals.

In this work, we studied the effect of uniaxial strain on the bulk photovoltaic effect in van der Waals layered semiconductor 3R-MoS_2. Without strain, 3R-MoS_2 has a noncentrosymmetric trigonal crystal structure (Fig.1 (a)). Although it exhibits the photoconductivity, which indicates the enhancement of conductivity under the illumination of light, zero-bias photocurrent is negligibly small (Fig. 1 (b)). By transferring the exfoliated flake of 3R-MoS_2 on a pre-patterned substrate consisting of two parallel steps and pushing it so that flake stretches and gets in contact with the bottom substrate part, we applied the uniaxial strain on 3R-MoS_2 (Fig. 1 (c)). In strained samples, symmetry of the crystal is reduced and electronic polarization appears (inset of Fig. 1 (c)). We found that zero-bias photocurrent is largely enhanced in such strained samples (Fig. 1 (d)). We confirmed that photocurrent appears when the light is illuminated at the center of the device away from the electrodes and flows only

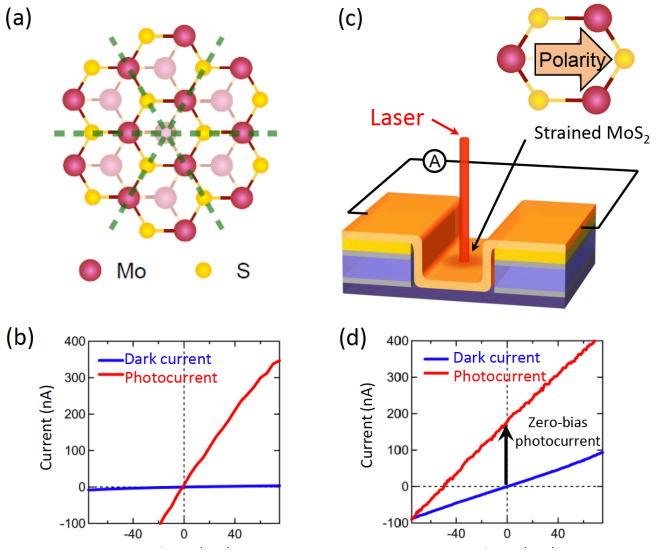

Fig. 1. (a)Crystal structure (top view) of 3R-MoS_2. Green dashed lines indicate the mirror planes. (b) The *I-V* characteristic of an unstrained 3R-MoS_2 device. (c) Schematic of photocurrent measurement in a strained 3R-MoS_2 device. (d) The *I-V* characteristic of a strained 3R-MoS_2 device.

along the direction parallel to the electronic polarization. It is also observed that the magnitude of the zero-bias photocurrent increases in a nonlinear manner with the value of uniaxial strain. These results implies that the observed zero-bias photocurrent is the intrinsic bulk photovoltaic effect and the emergence of the electronic polarization is essential to enhance the bulk photovoltaic effect.

We further studied the detailed light power dependence and photon energy dependence of the bulk photovoltaic effect. The light power dependence of the photocurrent shows the characteristic crossover, evolving from a linear relation to a nonlinear manner while increasing the light intensity. The photon energy dependence of the zero-bias photocurrent exhibits the non-monotonic behavior differently from the absorption spectrum. These behaviors can be well explained by the shift current, which is one of the origins of bulk photovoltaic effect related to the geometrical properties (Berry connection or shift vector) of the wave function and arises from the shift of the wave packet under the optical transition.

In summary, we have demonstrated the gigantic enhancement of bulk photovoltaic effect by uniaxial strain in van der Waals layered semiconductor 3R-MoS_2. This work clarifies the important role of symmetry reduction and the induced electric polarization for the large photocurrent generation, enriching our knowledge concerning the microscopic mechanism of bulk photovoltaic effect in non-centrosymmetric systems. Present results also indicate that strain application is a powerful method to control the symmetries, geometric properties of the electronic wave function, and resultant physical properties of flexible layered materials.

Reference
[1] Y. Dong, M. Yang, M. Yoshii, S. Matsuoka, S. Kitamura, T. Haswgawa, N. Ogawa, T. Morimoto, T. Ideue, and Y. Iwasa, Nat. Nanotechnol. **18**, 36 (2023).

Authors
Y. Dong[a], M. Yang[b,c], M. Yoshii[a], S. Matsuoka[a,d], S. Kitamura[a], T. Haswgawa[a], N. Ogawa[b], T. Morimoto[a], T. Ideue, and Y. Iwasa[a,b]
[a]The University of Tokyo
[b]RIKEN Center for Emergent Matter Science (CEMS)
[c]The University of Warwick
[d]Nagasaki University

Spin Hall Magnetoresistance in Quasi-Two-Dimensional Antiferromagnetic-Insulator /Metal Bilayer Systems

Kato Group

Recently, a novel type of magnetoresistance, called spin Hall magnetoresistance (SMR), has been attracting much attention. SMR was first observed in a normal metal (NM)/ ferromagnetic insulator bilayer [1] and subsequently in a NM/antiferromagnetic insulator (AFI) bilayer [2]. Because SMR reflects information on the FI magnetization or AFI Néel vector, it can be utilized for detecting the orientation of ordered spins in magnetic materials. Although the existing theory [1,3] succeeds in explaining the qualitative features of SMR measurements, it could not explain the temperature dependence of the SMR signal. Recently, a microscopic theory using Green's function has been constructed [4]. This microscopic theory describes SMR in terms of local spin susceptibilities of the FI(AFI). It can include dynamic processes such as magnon absorption and emission responsible for a nontrivial sign change in the SMR signal, which are neglected in the semiclassical theory.

In this study, we numerically calculated SMR by using a quantum Monte Carlo method [5] for a NM/AFI bilayer (see Fig. 1 (a)). We utilized an improved method for accurately obtaining the integral of the local spin susceptibilities from the QMC data without using numerical analytic continuation. We evaluated the detailed temperature dependence of SMR for S = 1/2 and S = 1 spin systems on a two-dimensional square lattice and a quasi-two-dimensional cubic lattice with a finite number of layers.

Figure 1 (b) shows the spin conductance, which is proportional to the SMR signal, for the S = 1/2 quasi-two-dimensional quantum Heisenberg model on a $16 \times 16 \times W$ (W = 2, 4, 6) cubic lattice. As the thickness W increases, the ordering temperature (indicated by the green arrows) increases. The spin conductance induced below the transition temperature becomes large while it vanishes above the transition temperature. We find that the peak of the spin conductance is greatly enhanced compared with that for a single-layer spin system (not shown). Although the maximum of the spin conductance increases with increasing thickness W, the difference between the results for W = 4 and 6 is much smaller than that for W = 2 and 4. Figure 1 (c) shows the SMR signal for the S = 1 quasi-two-dimensional quantum Heisenberg model on a $16 \times 16 \times W$ (W = 2, 4, 6) cubic lattice. As the thickness W increases, the ordering temperature (indicated by the green arrows) raises and the SMR signal becomes large. Above the transition temperature, the SMR signal becomes small but remains finite, in contrast with the case of S = 1/2. We showed that this feature can be understood well by the high-temperature expansion. As the temperature decreases below the ordering temperature, the SMR signal increases, takes a maximum roughly at three-fifths of the ordering temperature, and then decreases. The maximum value of the signal is rather larger than in the case of S = 1/2. At sufficiently low temperatures, the SMR signal becomes negative, as predicted by the spin-wave approximation. We also discussed the effect of the disordered exchange interactions.

In our study, we succeeded in clarifying the qualitative features of SMR based on the numerical results. These qualitative features are expected to be observed experimentally. Our simulation using a simplified model is expected to be a useful starting point for understanding SMR in quasi-two-dimensional quantum spin systems.

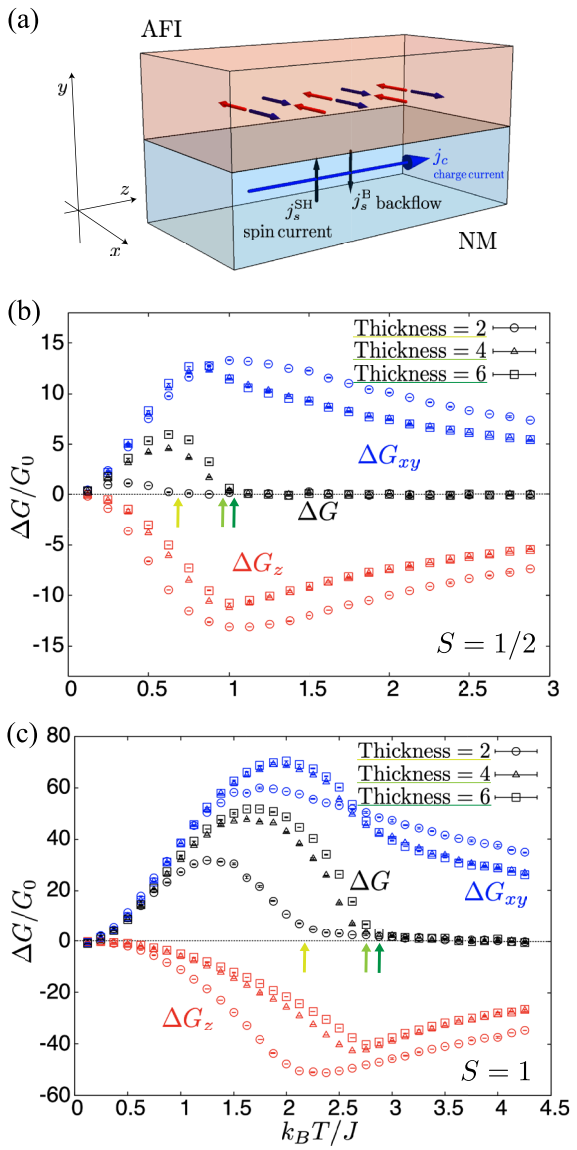

Fig. 1. (a) Illustration of spin Hall magnetoresistance. Spin absorption at the interface changes according to the orientation of the Néel vector of the antiferromagnetic insulator, and the magnitude of the magnetoresistance changes. (b,c) Temperature dependences of spin conductance ΔG are shown for (b) S = 1/2 and (c) S = 1 quantum Heisenberg model. The two contributions, ΔG_{xy} and ΔG_z, are plotted separately.

References

[1] H. Nakayama *et al*., Phys. Rev. Lett. **110**, 206601 (2013).
[2] D. Hou *et al*., Phys. Rev. Lett. **118**, 147202 (2017).
[3] Y. T. Chen *et al*., Phys. Rev. B **87**, 144411 (2013).
[4] T. Kato, Y. Ohnuma, and M. Matsuo, Phys. Rev. B **102**, 094437 (2020).
[5] T. Ishikawa, M. Matsuo, and T. Kato, Phys. Rev. B **107**, 054426 (2023).

Authors
T. Ishikawa, M. Matsuo, and T. Kato

Shear-Strain Controlled High-Harmonic Generation in Graphene

Kato and Akiyama Groups

Two-dimensional (2D) Dirac electrons in single-layer graphene have attracted much attention for their novel linear and nonlinear optical properties. One-atom-thick graphene exhibits universal frequency-independent light absorption, $\pi\alpha$ = 2.3%, where $\alpha = e^2/\hbar c \approx 1/137$ is the fine structure constant [1]. Ultrafast carrier dynamics on massless bands provide a variety of high-speed broadband optical responses. Further studies have targeted artificial control, modulation, or switching of these properties for potential applications in graphene-based optical devices. However, the robustness of optical transition probability $\pi\alpha$ inherent to 2D Dirac electrons makes the external control of optical responses highly challenging.

A graphene sheet has high flexibility and a shear strain of up to 27% can be reversibly applied to it [2]. This strain effect should be useful for control of the nonlinear optical responses of graphene. In this study [3], we theoretically demonstrated a significant enhancement or quenching of HHG over several orders of magnitude in graphene by tuning the shear strain and the incident-light polarization angle (Fig. 1 (a)).

We show the shear-strain dependences of the third and fifth harmonics in Fig. 1 (b) and (c). The red and green lines indicate the dependences for the different incident-light polarization angles, $\theta = 120^\circ$ and $\theta = 30^\circ$, respectively (for definition of theta, see Fig. 1 (a)). These two angles are regarded as the specific ones because they can yield the maximum and minimum intensities of the emitted harmonics (see insets in Fig. 1 (b) and (c)). Fig. 1 (b) and (c) show that, for $\theta = 120^\circ$, the third-order (fifth-order) harmonics are largely enhanced by around one order of magnitude at $\zeta \approx 0.13$ and 0.18, while they are quenched rapidly by around third (eight) orders of magnitude at $0.2 < \zeta < 0.27$ (red line), where ζ is the amplitude of the shear strain. The plots for $\theta = 30^\circ$ do not show this nonmonotonic behaviour; they only show an approximately monotonic decrease with increasing shear strain. By using linear response theory, we showed that the HHG enhancement came from the resonances at which the incident-light photon energy matches the saddle-point energy or the band gap [3]. In addition, the dipole moment near the saddle point (or the band gap) plays an important role in the polarization angle dependence of this enhancement. Strong quenching of HHG was induced by rapid growth of the band-gap energy with increasing shear strain.

In conclusion, we theoretically investigated the linear and nonlinear optical responses of graphene distorted by shear strain. Using the tight-binding model, we clarified that tuning both the shear strain and the polarization angle of the incident THz light enables a significant enhancement or quenching of HHG. Our findings suggest the possibility of using shear strain to control HHG in graphene and pave the way for optical nanotechnology of single-layer materials.

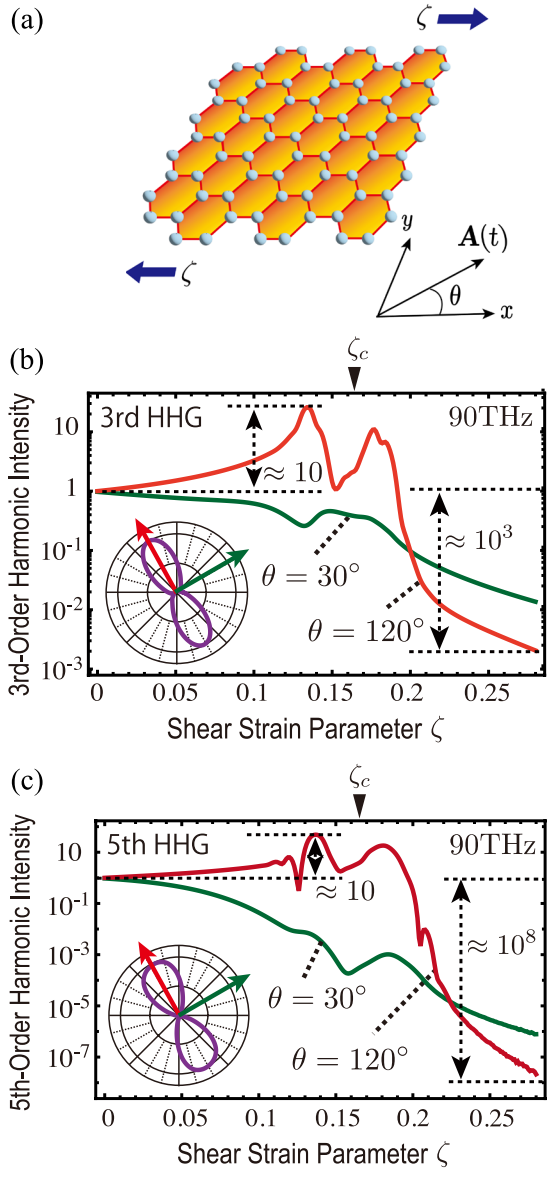

Fig. 1. (a) Schematic figure of lattice structure of graphene under shear strain. The amplitude of the shear strain is represented by ζ and the vector potential of the incident light is denoted as $A(t)$, whose tilt angle measured from the armchair axis is described by θ (see the inset). (b) Shear strain dependence of the third- and fifth-order harmonics. The red and green lines indicate the high-harmonic intensities for the incident-light angles $\theta = 120^\circ$ and $\theta = 30^\circ$, respectively. The polarization angle dependences of the third and fifth harmonics for $\zeta = 0.12$ are shown in the insets. The critical strength of the shear strain for a band gap to form is described by ζ_c.

References

[1] R. R. Nair, P. Blake, A. N. Grigorenko, K. S. Novoselov, T. J. Booth, T. Stauber, N. M. Peres, and A. K. Geim, Science **320**, 1308 (2008).

[2] Z. Peng, X. Chen, Y. Fan, D. J. Srolovitz, and D. Lei, Light: Sci. Appl. **9**, 190 (2020).

[3] T. Tamaya, H. Akiyama, and T. Kato, Phys. Rev. B **107**, L081405 (2023).

Authors

T. Tamaya, H. Akiyama, and T. Kato

Visualizing Magnetization c Domain Structure with Heat Injection Using Atomic Force Microcopy

Otani Group

Magnetic imaging plays a crucial role in studying the magnetism of materials. Its significance has been growing with the rapid development of topological magnetic materials. For instance, the magnetic domain structure of the antiferromagnetic Weyl semimetal Mn_3Sn [1] is intriguing from the magnetothermoelectric application point of view.

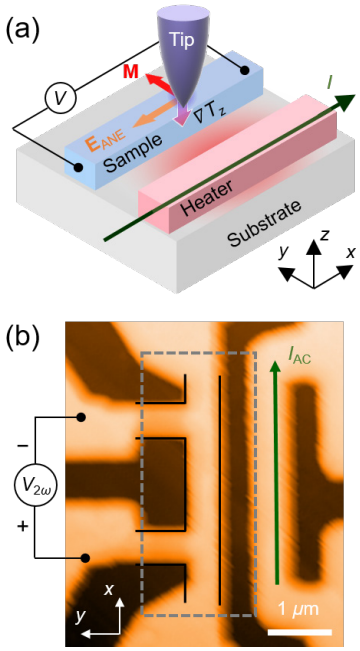

Fig. 1. (a) Conceptual drawing of magnetic imaging. (b) Device structure and electric configuration of the measurement.

However, the methods with enough high spatial resolution usually require costly instruments. Here, we report a simple magnetic imaging method using an atomic force microscope (AFM) with a sub-100-nm resolution, in which we measure the locally induced anomalous Nernst effect (ANE).

Figure 1(a) illustrates the concept of our method. The Joule effect of the heater causes a non-equilibrium temperature distribution in the sample nanowire. An AFM tip contact creates a local vertical temperature gradient $\nabla_z T$ in a sample. The ANE is expressed as $E_{\mathrm{ANE}} = S_{\mathrm{ANE}}(m \times \nabla T)$, where E_{ANE}, S_{ANE}, m are the electric field induced by ANE, the magnitude of ANE, and the unit vector of the magnetization, respectively. If the magnetization under the tip points to the wire width direction (the y-direction), the ANE causes a voltage along the x-direction. Therefore, the tip-induced ANE voltage represents the y-component of the local magnetization.

We demonstrate this method on the ferromagnetic Weyl semimetal Co_2MnGa that exhibits large ANE ($S_{\mathrm{ANE}} \sim 5\ \mu$V/K)

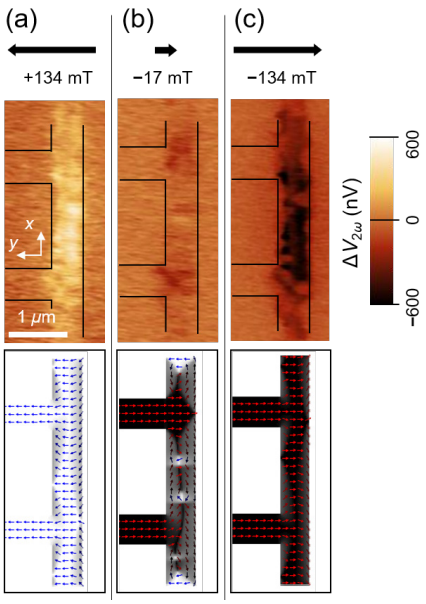

Fig. 2. The results of anomalous Nernst voltage mapping with (a) +134 mT, (b) −17 mT and (c) −134 mT.

[2]. The topographic image of the sample and the electric measurement configuration are shown in Fig. 1(b). We apply an alternating current to the heater and measure the voltage across the sample wire at the second harmonic frequency. We map the voltage during the scan with the contact mode. We conduct the experiment in an atmosphere at room temperature. The result of the voltage mapping Figure 2(a), (b), and (c) represents the results under the external magnetic field along the y-direction of +134 mT, −17 mT, and −134 mT, respectively. With +134 mT, a uniformly positive voltage is obtained. The magnitude of the signal is proportional to the square of the current. The signal reverses its sign with −134 mT. These results indicate that the voltage is attributable to the ANE. With −17 mT, a pair of bright and dark spots (positive and negative voltage) appeared near the center of the sample wire. This reflects the presence of a 180° magnetic domain wall. The bottom row of Fig. 2 shows the results of micromagnetic simulation in the Co_2MnGa with each magnetic field obtained by OOMMF. One can see a good agreement between the experimental and simulation results. We estimated the spatial resolution to ~ 80 nm from the edge response of the ANE voltage. Using same technique, we saw a magnetic signal on the permalloy ($Ni_{80}Fe_{20}$) nanowire. Therefore, our method applies to the antiferromagnetic Weyl semimetal Mn3Sn ($S_{\mathrm{ANE}} \sim 0.5\ \mu$V/K).

We develop a simple method for magnetic imaging [3]. Our method only requires a conventional atomic force microscope with a high spatial resolution. Moreover, our technique can apply to antiferromagnetic Weyl semimetals that exhibit the anomalous Nernst effect.

References

[1] S. Nakatsuji and R. Arita, Annu. Rev. Condens. Matter Phys. **13**, 119 (2022).
[2] A. Sakai *et al.*, Nat. Phys. **14**, 1119 (2018).
[3] N. Budai, H. Isshiki, R. Uesugi, Z. Zhu, T. Higo, S. Nakatsuji, and Y. Otani, Appl. Phys. Lett. **122**, (2023).

Authors
H. Isshiki, and Y. Otani

Microscopic Views of Quantum Phase Transition in Disorder-Controlled 2D Superconductors

Hasegawa Group

Disorder-induced superconductor-insulator transition (SIT) in the two-dimensional (2D) systems has been a subject of extensive studies as one of typical examples of quantum phase transitions (QPT). Recent advancements in fabricating highly crystalline 2D systems revealed the unexpected quantum phases, such as anomalous metallic state and quantum Griffiths phase, around QPT. The origins of the new quantum phases are still uncovered partly because of lack of microscopic pictures. Here, by performing scanning tunnelling spectroscopy (STM) at low temperature (0.36 K) on highly-crystalline monoatomic-layer superconductors, we elucidated these quantum phases in real space microscopically.

In the present work we used one of the Pb-monolayer superconducting phases called striped incommensurate (SIC) phase formed on vicinal Si(111) substrates. On the vicinal substrates single-layer-height steps, which work as a disorder [1,2], are regularly aligned, and the density of steps can be

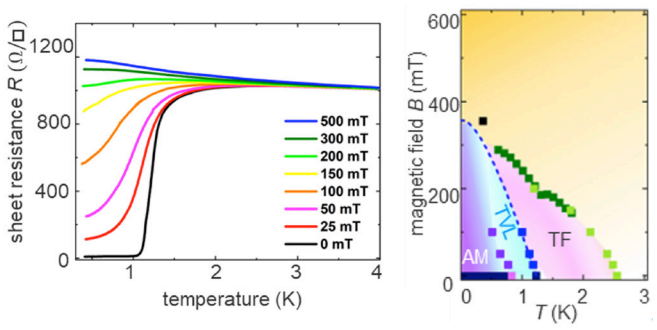

Fig. 1. (left) Temperature dependence of sheet resistance R measured on the 1.1°-tilted vicinal sample under out-of-plane magnetic fields of 0, 25, 50, 100, 150, 200, 300 and 500 mT. (right) B-T phase diagram obtained from the data shown in the left panel. AM: anomalous metallic phase, TVL: thermal vortex liquid phase, TF: thermal-fluctuation-induced metallic phase..

controlled precisely with the miscut angle. We investigated how the disorder in the superconducting layers affects the presence of the quantum phases.

First we performed *in situ* (in ultrahigh vacuum) transport measurements on the SIC phases formed on 1.1°-tilted vicinal substrates (Fig. 1). The terrace spacing for the vicinal substrate is 16 nm, shorter than the coherence length of the system (38 nm). The superconducting critical temperatures T_c of the vicinal samples are 1.21 K, slightly lower than the flat sample (1.53 K). Under out-of-plane magnetic fields below the critical field B_{c2}, the sample exhibits non-zero resistance near zero temperature, indicating the presence of anomalous (quantum) metallic phase, which is often explained with the quantum motion of vortices. From the Arrhenius plots of the sheet resistance R, we determined the crossover temperature between the regions where the quantum and thermal vortex motions are dominant.

Outside of the superconducting regime, metallic phases ($dR/dT > 0$) are observed. Whereas the thermal-fluctuation-induced metallic (paraconductivity) phases are found above T_c, the quantum-fluctuation (QF)-induced metallic phase, which appears above B_{c2} near $T = 0$, appears only on the flat sample, was not observed on the vicinal sample. The absence of the QF-induced metallic phase on the step-abundant sample is consistent with the fact that the QF-induced metallic phase, which is often attributed to quantum Griffith phase, is only observed on highly-crystalline monolayer samples.

Then, we performed STM observation at low temperature (T = 0.36 K). Figure 2 shows the results taken on the vicinal sample. Figure 2(a) is an STM image showing equally-spaced steps on the surface. Figure 2(b)-2(l) are maps showing the spatial distribution of the superconducting gap under various out-of-plane magnetic fields B. At B = 120 mT, individual oval vortices elongated along the steps are observed. The oval shape is due to the Josephson

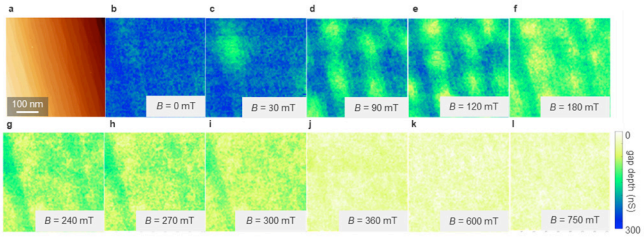

Fig. 2. (a) STM image taken on Pb monoatomic-layer SIC phase formed on 1.1°-tilted vicinal Si(111) substrate. (b-l) Superconducting gap depth maps under various out-of-plane magnetic fields on the same area as (a).

coupling at the steps and explained as Josephson-Abrikosov vortices [2]. By increasing B to 180 mT, vortices are significantly overlapped each other but still individual vortices are recognized, but at B = 270 mT individual vortices are not observable any more. B_{c2} can be estimated from the gap evolution with B outside of the vortices and found B_{c2} = 355 mT, which is consistent with that obtained by the transport measurement (Black square in the phase diagram of Fig. 1 corresponds to the B_{c2} by STM.). In the range of 270 mT < B < B_{c2}, the density of vortices should increase with B and in fact averaged gap depth decreases, but individual vortices cannot be seen. The indistinct vortices are, therefore, due to liquidation of vortices. Above B_{c2}, we still observed the gap remaining, and the pseudo gap disappears around B = 500 mT.

According to the phase diagram obtained by the transport measurement (right panel of Fig. 1), under 30 mT < B < 120 mT finite resistance is observed and thus anomalous metallic phase should be there at T = 0.36 K. However, in STM, we observed individual vortices, indicating the presence of short-range order of the vortex arrangement, at least. The regime is, therefore, the quantum creep phase, and the finite resistance is likely generated due to the vortex motions induced by infinitesimal current for the transport measurement.

We performed the same measurements on the flat sample and basically the same results were obtained in the low B range. Curiously, however, the vortex liquid phase was not observed on the flat sample. The vortex liquidation, which we believe induced by the quantum fluctuation, occurs only under the presence of phase fluctuation induced by the disorder.

Under B higher then B_{c2}, we observed a pseudo gap on both flat and vicinal samples. This implies that the localized Cooper pairs are formed, presumably by quantum fluctuation, regardless of the degree of disorder. Depending on the degree of disorder, however, the amount of the localization is different, making the system metallic or insulating depending on the amount of disorder.

References
[1] S. Yoshizawa *et al*., Phys. Rev. Lett. **113**, 247004 (2014).
[2] Y. Sato *et al*., Phys. Rev. Lett **130**, 106002 (2023).

Authors
Y. Sato, M. Haze, S. Yoshizawa[a], T. Uchihashi[a] and Y. Hasegawa
[a]National Institute for Materials Science

Machine Learning for Structural Phase Mapping

Lippmaa Group

Structural phase analysis in thin film materials development is usually done by ex-situ x-ray diffraction (XRD) after the film growth is finished. The XRD analysis typically takes longer than the film synthesis and the XRD analysis provides an average composition of the whole film volume without being able to distinguish which phases that occur at the surface or at the substrate interface. An alternative structure analysis method is in-situ reflection high-energy electron diffraction (RHEED), which provides structural information on the surface of the film in real time during growth. While this makes RHEED an attractive alternative to XRD, manual

analysis of RHEED patterns to determine the phase composition is generally time-consuming and thus rarely used for contemporaneous structure analysis with film growth.

We have developed a machine learning workflow to automatically detect and locate various diffraction features in complex diffraction patterns. We use the U-Net neural network segmentation algorithm to quickly determine where diffraction spots and streaks occur in a diffraction pattern, as illustrated in Fig. 1. The neural network has to be trained before such image segmentation is possible. For this purpose, we collect a large number of visually different diffraction patterns and hand-label those training patterns, manually marking the position of each diffraction spot and streak. The training image set is then used to train the U-Net to recognize the desired features in typical RHEED patterns. As shown in Fig. 1, U-Net can reliably distinguish between overlapping spots and streaks and can find even very weak features that are difficult to detect by eye.

The U-Net segmentation tool produces mask patterns. As the next step in the workflow, the original image intensity distribution is examined in each mask area. For example, it is possible to integrate the intensity in the vertical direction in each mask area and examine the resulting cross-section plots by peak fitting to determine accurate horizontal diffraction feature positions. The feature spacing corresponds to the distance between neighboring reciprocal space points and can thus be used to calculate the in-plane lattice parameter. In case the surface contains a mixture of phases, multiple spot or streak periodicities will appear on the surface. An iterative approach was developed to extract all base periodicities from a complex image, providing a list of periodicities. The total diffraction intensity corresponding to each bas distance is then used to calculate the phase composition ratios.

A series of thin film FeO_x samples was synthesized over a broad range of film growth temperatures and ambient oxygen pressures. The RHEED patterns of all films were analyzed using the automated composition analysis workflow. This produced for each synthesis phase space point a descriptor containing information on the phase lattice parameters and the associated relative diffraction intensities. Clustering was then used to form a phase map as shown in Fig. 2, where a pie diagram at each synthesis point represents the relative intensities of each clustered lattice parameter.

The mapping result shows that hematite Fe_2O_3 (green) dominates the film composition in the 600 to 800 °C range, while magnetite Fe_3O_4 (pink) appears at both lower and higher temperatures. This result was verified by later x-ray

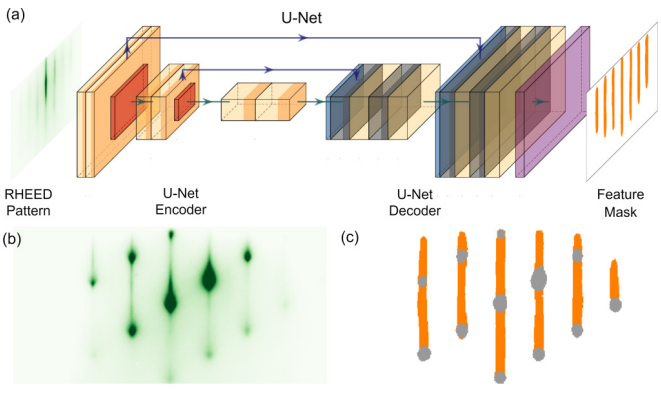

Fig. 1. (a) Schematic diagram of the U-Net model used for semantic segmentation of RHEED patterns. (b) and example pattern of a hematite film. (c) Masks for diffraction spots (gray) and streaks (orange) generated by the neural network model.

Fig. 2. A phase diagram constructed by automated RHEED pattern analysis for FeO_x phase formation in thin films grown at various oxygen pressures and temperatures. The marker colors correspond to various lattice periodicities. The center region is mostly hematite (green), while magnetite (pink) appears at both low and high growth temperatures.

diffraction analysis. Under thermodynamic equilibrium conditions, a monotonic change from magnetite at higher growth temperatures to hematite at lower temperatures would have been expected. The non-monotonic phase composition variation shows the importance of kinetic effects in thin film growth.

The RHEED phase mapping thus produces an equivalent result to XRD analysis, but RHEED mapping can be done in-situ in near-real-time. The machine learning workflow thus creates a new way to use RHEED for automated phase formation analysis and real-time phase evolution tracking during thin film growth.

Reference

[1] H. Liang, V. Stanev, A. G. Kusne, Y. Tsukahara, K. Ito, R. Takahashi, M. Lippmaa, and I. Takeuchi, Phys. Rev. Materials **6**, 063805 (2022).

Authors

H. Liang[a], V. Stanev[a,b], A. G. Kusne[a,c], Y. Tsukahara[d], K. Ito[d], R. Takahashi[d], M. Lippmaa, and I. Takeuchi[a]

[a]University of Maryland
[b]AstraZeneca
[c]NIST
[d]Nihon University

Elucidation of the Atomic-Scale Processes of Dissociative Adsorption and Spillover of Hydrogen on the Single Atom Alloy Catalyst Pd/Cu(111)

Yoshinobu and Ozaki Groups

The utilization of hydrogen in industry has become more important for our modern society because many indispensable processes consist of chemical reactions involving hydrogen: synthesis of chemical feedstocks such as methanol and ammonia, petroleum refining, energy sources through fuel cell systems, and so forth. In these reactions, dissociation of molecular hydrogen is an essential elementary step in hydrogenation reactions, where the active sites for hydrogen dissociation are necessary. In recent years, single atom alloy catalysts (SAACs) have been attracting much attention due to their excellent properties, such as high activity/selectivity and resistance to deactivation via coke formation or CO poisoning. In SAACs, active metal atoms are highly diluted and atomically dispersed on an inert but selective metal surface. Several previous studies have shown that the Pd/

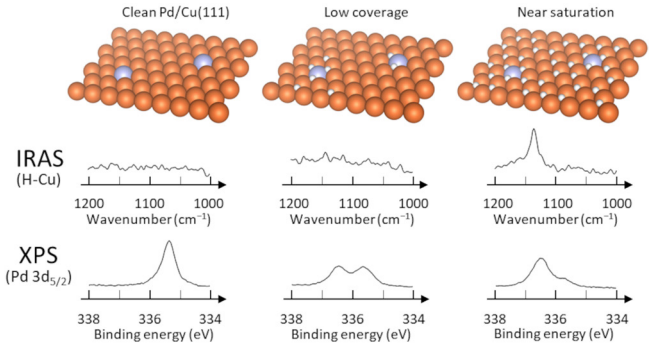

Fig. 1. (Up) Schematic models of the dissociative adsorption and spillover of hydrogen on Pd/Cu(111) as a function of coverage (Middle) Vibrational spectra of the Cu-H stretching mode (Bottom) Photoelectron spectra of Pd3d$_{5/2}$

Cu SAAC shows excellent activity for hydrogen dissociation and hydrogenation reactions. On the Pd/Cu SAACs, the hydrogen spillover from Pd sites onto Cu host surfaces is a vital process for selective hydrogenation because it has been considered that the reaction proceeds on the Cu surface which weakly interacts with the product molecules.

We investigated the dissociative adsorption of hydrogen and the subsequent spillover process on the Pd/Cu(111) surface using infrared reflection absorption spectroscopy (IRAS), temperature programmed desorption (TPD), and high-resolution X-ray photoelectron spectroscopy (HR-XPS), as well as density functional (DFT) calculations [1]. The hydrogen spillover onto Cu(111) was successfully observed in real time using time-resolved IRAS measurements. The chemical shifts of Pd 3d$_{5/2}$ indicate that molecular hydrogen is dissociated and adsorbed at the Pd site. In addition, "two-step" chemical shifts of the Pd 3d$_{5/2}$ binding energy were observed as a function of hydrogen exposure. The DFT calculation revealed that the "two-step" chemical shifts originate from the charge transfer (CT) from Pd to hydrogen; initially hydrogen atoms are directly adsorbed at the Pd site, and thereafter a significant amount of additional hydrogen atoms are adsorbed at the Cu sites in which CT occurs in an indirect manner. Based on the present experimental and theoretical results, we propose the following mechanism of the hydrogen dissociation and spillover process on Pd-Cu(111) : (i) a hydrogen molecule is dissociated at a Pd site, and the hydrogen atoms are adsorbed on the Pd site, (ii) the number of hydrogen atoms on the Pd site increases up to three, and (iii) the additional hydrogen atoms spill over onto the Cu surface.

Reference
[1] W. Osada, S. Tanaka, K. Mukai, M. Kawamura, Y.H. Choi, F. Ozaki, T. Ozaki, and Jun Yoshinobu, Phys. Chem. Chem. Phys. **24**, 21705 (2022).

Authors
W. Osada, S. Tanaka, K. Mukai, M. Kawamura, Y.H. Choi, F. Ozaki, T. Ozaki, and J. Yoshinobu

Thought Experiment of the Activity of an Oxide Electrode

Sugino Group

While a great deal of attention has been given to the computational design of functional materials, the degree of freedom is overwhelming when dealing with the heterogeneous interfaces of defective materials. Typical example is the defective oxides interfaced with solutions used for the electrocatalysis application. Recent experiments show that both zirconia and titania cathodes provide enhanced electromotive force of fuel cells when they contain nitrogen impurities and oxygen vacancies, but the microscopic structure of the electrode-electrolyte interface is not well understood. In this context, we use the large supercomputers such as Fugaku and the recently developed programs such as abICS [1] to perform ab initio Monte Carlo (MC) and molecular dynamics simulations to model the interface by sampling unprecedentedly large degrees of freedom. Note that abICS does not simply generate the ab initio trajectories, but also help enhance the sampling by machine learning the generated trajectories to significantly speed up the simulation. We used them to address the problem of understanding the reason for the improved fuel cell efficiency. In our approach, we first simulated the zirconia surface and then the zirconia-water interface.

Our previous simulation has revealed that an oxygen vacancy can be stabilized when doped with two times denser nitrogen impurities because of the charge compensation effect. The surface simulation showed that the vacancies are distributed not only at the surface but also in the subsurface regions, while the nitrogen impurities do not favor the surface sites. Based on this result, we reduced the size of the model surface so that we can examine all possible configurations of the ORR intermediates, i.e., O_2*, O_2H*, OH*, and O*, where * means adsorbed species. The resulting adsorption energies were used to obtain the free energy profile. The result showed that an oxygen molecule can be efficiently reduced to form water molecules on the vacancy site, with the activity comparable to that of the platinum electrode [2]. The activity was estimated thermodynamically using the empirical assumption that the barrier existing between the reaction intermediates does not play a role. Importantly, the estimated activity was found to be comparable to that of the non-defective surface. This result should be interpreted with caution. Considering the low availability of the active defects, we can conclude that the overall rate of ORR is likely to be higher for the non-defective surface, although we cannot rule out the possibility that we have missed important configurations due to the finite cell size and time used for the simulation. The apparent inconsistency with experiments that the efficiency of the fuel cell is increased by introducing the defects can be explained if the carrier supply is significantly increased by doping. This will be the case if defect induced

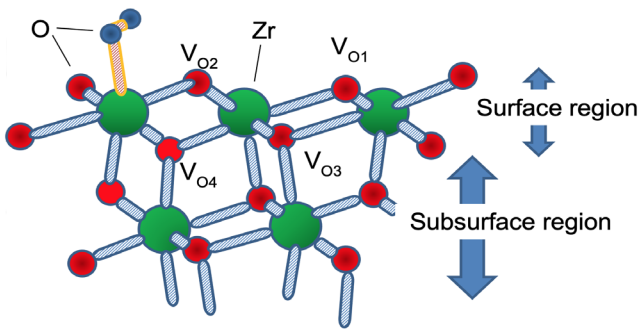

Fig. 1. (Schematic view) Part of the 2 × 1 slab model of the defective tetragonal ZrO_2(101) surface where one O_2 molecule (blue spheres) is adsorbed on a surface Zr atom (green) surface. We have examined all possible paths for the oxygen reduction reaction where the adsorbed O_2 is reduced to form a water molecule. The defect site was modeled by removing a surface O atom, VO1 and VO2, and substituting a subsurface O atom with a N impurity.

gap states are extended in the sample. With this in mind, we are now theoretically investigating the electrostatic potential profile to see how the carrier path can be facilitated.

In the above surface simulation, we have neglected the solvation effect. Water molecules can be adsorbed on the zirconia surface as a molecule or as dissociated species, OH* and H*, blocking the incoming oxygen molecule to be adsorbed. This possibility was investigated using the machine-learned potential developed with abICS. Based on many nanosecond trajectories, we found that water molecules do not favor the surface vacancy site, while they favor reactive Zr sites when no defects are introduced. This is likely to be an indirect indication that the blocking effect is significantly different between the defective and pristine surfaces. Further simulations are now in progress to make a conclusion about the solvation effect.

References

[1] https://www.pasums.issp.u-tokyo.ac.jp/abics/

[2] S. Muhammady, J. Haruyama, S. Kasamatsu, and O. Sugino, J. Phys. Chem. C**126**, 15662 (2022).

Authors

S. Muhammady, A. Nakanishi, A. F. Flaviano, J. Haruyama, S. Kasamatsu[a], and O. Sugino.

[a]Yamagata University

Study on the Channel Gating Mechanism of Channelrhodopsin C1C2

Akiyama and Inoue Groups

Channelrhodopsins (ChRs) are members of microbial rhodopsins that function as light-gated cation channels. ChRs are composed of seven transmembrane (TM) helices and an all-*trans*-retinal chromophore which is covalently bound to the seventh TM helix via a protonated Schiff base linkage. Light absorption induces the isomerization of the retinal chromophore from the all-*trans* to the 13-*cis* form leading to the subsequent conformation change of the protein moiety opening the ion-transport channel connecting the extracellular and cytoplasmic solvents. Recently, ChRs are being used widely in optogenetics to control neural activity in an animal body. Whereas high-functional ChR proteins are being strongly demanded to realize efficient and low-invasive optogenetics, the lack of understanding of its channel-gating mechanism is inhibiting rational and precise protein engineering to improve the functionality of ChRs. The structural information of the open state of ChR

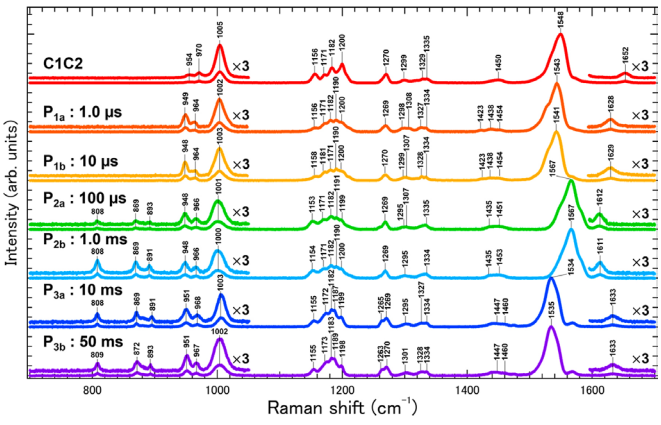

Fig. 1. Time-resolved resonance Raman spectra of each state of C1C2

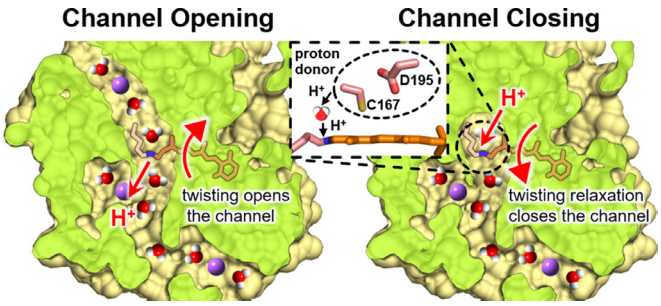

Fig. 2. Channel gating mechanism of C1C2

is indispensable to clarify the mechanism. However, it was difficult due to the inhibition of the channel opening by the tight packing of protein molecules in the crystal phase for the X-ray crystallographic analysis.

To overcome this difficulty, we studied the channel opening and closing processes of C1C2, one of the best characterized ChRs whose three-dimensional structure was first solved, by time-resolved resonance Raman spectroscopy, laser flash photolysis, and laser electrophysiology. Especially, time-resolved resonance Raman spectroscopy can selectively obtain detailed information on the chemical bonds of the retinal chromophore based on its vibrational modes. However, time-resolved resonance Raman spectroscopy generally requires a large amount of protein sample which is difficult to prepare for C1C2. We avoided this problem by developing a new Raman microspectroscopy system using semiconductor lasers, acoustic-optics modulators (AOM), an optical objective lens, and an automated optical stage. As a result, we succeeded in obtaining the resonance Raman spectra of the initial and all photointermediate states of C1C2 and revealed the enhancement of the hydrogen-out-of-plain mode of the retinal chromophore after the photoexcitation of C1C2 indicating the polyene chain of the retinal is more twisted compared with the dark state. The twisting of the retinal is maximized in the full-open state of C1C2. Hence, the channel gate in C1C2 is opened by the steric repulsion between the retinal chromophore and transmembrane helices as previously suggested by the quantum-mechanics/molecular-mechanics calculation [1] and time-resolved X-ray crystallographic study [2] on the pre-opened state. On the other hand, the shift and broadening of the C=N stretching vibration band revealed the switching of the hydrogen-bonding partner of the retinal Schiff base from the counterion to a water molecule during the channel opening. Furthermore, the laser flash photolysis and laser electrophysiology measurements revealed that, while the channel opening kinetics did not alter between H_2O and D_2O solvents, the rate of channel closing was significantly slowed in D_2O compared to H_2O. This result indicates that the protonation of the retinal chromophore relaxes the twisted polyene chain leading to the channel closing.

This study provided a new understanding of the channel gating mechanism of ChR in which the channel opening is induced by the retinal twisting and the closing rate is regulated by the proton transfer between the protein moiety and the chromophore [3]. The development of novel functional ChRs based on this understanding in the near future is highly expected.

References

[1] C. Cheng, M. Kamiya, M. Takemoto, R. Ishitani, O. Nureki, N. Yoshida, and S. Hayashi, Biophys. J. **115**, 1281 (2018).

[2] K. Oda, T. Nomura, T. Nakane, K. Yamashita, K. Inoue, S. Ito, J. Vierock, K. Hirata, A. D. Maturana, K. Katayama, T. Ikuta, I. Ishigami,

T. Izume, R. Umeda, R. Eguma, S. Oishi, G. Kasuya, T. Kato, T. Kusakizako, W. Shihoya, H. Shimada, T. Takatsuji, M. Takemoto, R. Taniguchi, A. Tomita, R. Nakamura, M. Fukuda, H. Miyauchi, Y. Lee, E. Nango, R. Tanaka, T. Tanaka, M. Sugahara, T. Kimura, T. Shimamura, T. Fujiwara, Y. Yamanaka, S. Owada, Y. Joti, K. Tono, R. Ishitani, S. Hayashi, H. Kandori, P. Hegemann, S. Iwata, M. Kubo, T. Nishizawa, and O. Nureki, eLife **10**, e6238 (2021).
[3] K. Shibata, K. Oda, T. Nishizawa, Y. Hazama, R. Ono, S. Takaramoto, R. Bagherzadeh, H. Yawo, O. Nureki, K. Inoue, and H. Akiyama, J. Am. Chem. Soc., doi: 10.1021/jacs.3c01879 (2023).

Authors
K. Shibata, K. Oda[a], T. Nishizawa[a], Y. Hazama, R. Ono, S. Takaramoto, R. Bagherzadeh, H. Yawo, O. Nureki[a], K. Inoue, and H. Akiyama
[a]The University of Tokyo

Non-Invertible Duality Transformation Between SPT and SSB Phases

Oshikawa Group

Symmetry-Protected Topological (SPT) phases are one of the central issues in contemporary quantum many-body physics. While the concept of SPT phases was established after the discovery of topological insulators, which are the free electron version of SPT phases, a prototypical example of the bosonic SPT phases, the Haldane gap phase, was found much earlier. In 1992, Kennedy and Tasaki constructed a non-local unitary transformation that maps between a $\mathbb{Z}_2\times\mathbb{Z}_2$ spontaneously symmetry breaking phase and the Haldane gap phase on an open spin chain [1,2]. This gave a unified understanding of the exotic natures of Haldane gap phase, narrowly missing the clear recognition of concept of the SPT phases.

Since the discovery of the concept of the SPT phases in 2009, significant progress has been made on many fronts. In particular, systematic classifications in general dimensions have been studied, uncovering the deep relation to topological quantum field theory and algebraic topology. Given the history, it would be worthwhile to revisit the Kennedy-Tasaki transformation, which played a significant role in understanding the Haldane gap phase 30 years ago, from the modern perspective.

To this end, in this work [3] we demonstrate that the Kennedy-Tasaki transformation can be defined on closed chains by sacrificing unitarity, or by expanding the Hilbert space by including "twist" sectors corresponding to different boundary conditions. This is shown for both the original Kennedy-Tasaki transformation on $S = 1$ chain and for its generalization on $S = 1/2$ chain. In both cases, the closed chain version of the Kennedy-Tasaki transformation is a non-unitary transformation and satisfy the non-invertible fusion rules, as in the famous Kramers-Wannier duality transformation. Such non-invertible duality transformations generalizing the Kramers-Wannier duality have been extensively discussed in recent years, both in (1 + 1) and higher dimensions. When the system is invariant under the duality transformation, the operator representing the transformation becomes a non-invertible symmetry of the system. Indeed, we reveal the close connection between the Kramers-Wannier and Kennedy-Tasaki dualities; in particular, we show that Kennedy-Tasaki duality can be constructed in terms of the Kramers-Wannier duality in field theory and on $S = 1/2$ chain.

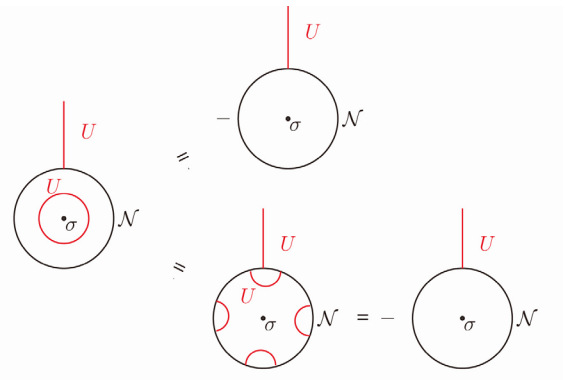

Fig. 1. A graphical illustration for the fusion rule between the Kramers-Wannier duality $\mathcal{N}$ and the global spin-flip operator U in the twisted sector, which is implemented by the twist operator σ. This type of relations is also relevant for Kennedy-Tasaki transformation.

Although the Kennedy-Tasaki transformation on $S = 1$ chain and that on $S = 1/2$ chain can be shown to be equivalent, the construction on $S = 1/2$ chain is more convenient for further applications, because the degrees of freedom charged under two $\mathbb{Z}_2$'s are decoupled; the first and the second groups of $S = 1/2$ are charged under separate $\mathbb{Z}_2$'s respectively. Moreover, the decoupling between degrees of freedom admits a more convenient interpretation of twisted gauging, similarly to the Kramers-Wannier duality transformation which implements gauging of the $\mathbb{Z}_2$ global symmetry. This interpretation also facilitates the construction of new models with interesting topological features. In particular, we utilize Kennedy-Tasaki transformation on $S = 1/2$ chain to systematically construct a series of gapless SPT phases, not only those have been recently explored, but also uncovering new ones. Our work opens up a new approach to the study of gapless SPT phases, which are at the forefront of the current quantum many-body problem.

References
[1] T. Kennedy and H. Tasaki, Phys. Rev. B **45**, 304 (1992); Commun. Math. Phys. **147**, 431 (1992).
[2] M. Oshikawa, J. Phys. Condens. Matter **4**, 7469 (1992).
[3] L. Li, M. Oshikawa, and Y. Zheng, arXiv:2301.07899 (2023).

Authors
L. Li, M. Oshikawa, and Y. Zheng[a]
[a]Kavli IPMU (and ISSP)

Pressure-Induced Superconductivity up to 9 K in the Quasi-One-Dimensional KMn_6Bi_5

Uwatoko Group

Unconventional superconductivity beyond the Bardeen-Cooper-Schrieffer theory usually emerges on the border of long-range antiferromagnetic order as exemplified by the cuprate, iron-pnictide, and heavy-fermion superconductors. In these cases, the enhanced magnetic fluctuations are believed to be the binding glue of Cooper pairs. As such, it is expected to find unconventional superconductivity in the vicinity of the antiferromagnetic quantum critical point (QCP), which can be achieved by employing external tuning parameters such as chemical doping and applying physical pressure. By following this approach, we discovered the first Mn-based superconductor MnP by suppressing its helimagnetic order via the application of high pressure, even though the Mn-based superconductor is rare owing to the strong magnetic pair-breaking effect. Its superconducting transition temperature Tc ≈ 1 K is low and the superconductivity

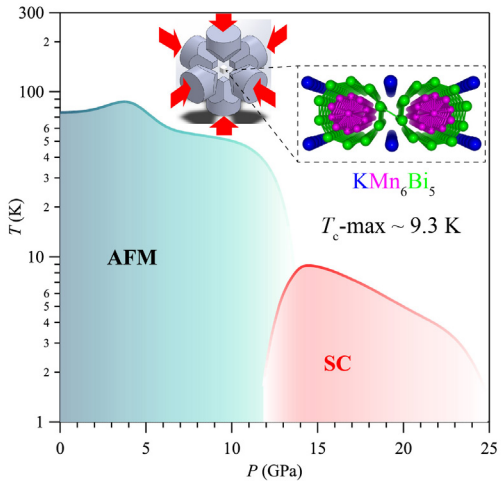

Fig. 1. Temperature-pressure phase diagram of KMn_6Bi_5. Inset shows the Q1D crystal structure of KMn_6Bi_5.

only appears in a narrow pressure range around Pc ≈ 8 GPa where the helimagnetic order just vanishes. Since then, we have been devoted to find more Mn-based superconductors with higher T_c. In this regard, we pay special attention to the ternary or complex Mn-based magnetic materials with low-dimensional structures, in which the enhanced magnetic fluctuations are expected to promote stronger superconducting pairing and thus higher T_c in comparison to the three-dimensional MnP. After seven-year endeavor, we recently discovered the first ternary Mn-based superconductor KMn_6Bi_5 [1].

KMn_6Bi_5 is a newly synthesized ternary compound with a quasi-one-dimensional (Q1D) monoclinic structure featured by the presence of infinite $[Mn_6Bi_5]^-$ columns along the b-axis as shown in the inset of Fig. 1. These columns are composed of an outer nanotube of Bi atoms surrounding an inner Mn–Mn bonded metallic core. At ambient pressure (AP), KMn_6Bi_5 undergoes an antiferromagnetic transition at $T_N \approx 75$ K, which is manifested as a pronounced anomaly in resistivity and magnetic susceptibility. Curie–Weiss fitting to the paramagnetic susceptibility above T_N yield a relatively small effective moment of Mn, i.e., 1.4-1.6 μB, signaling an itinerant nature of the magnetism similar to MnP. First-principles calculations have revealed that the density of states at the Fermi level are dominated by the Mn-3d electrons and the helical antiferromagnetic structures are stable.

By measuring resistance and ac magnetic susceptibility under hydrostatic pressures up to 14.2 GPa in a cubic anvil cell apparatus, we find that its antiferromagnetic order is first enhanced moderately and then suppressed completely at a critical pressure of $P_c \approx 13$ GPa, around which bulk superconductivity emerges and exhibits a domelike $T_c(P)$ with the maximal $T_c^{onset} \approx 9.3$ K achieved at 14.2 GPa. As shown in Fig. 1, the close proximity of superconductivity to a magnetic instability in the temperature-pressure phase diagram of KMn_6Bi_5 resembling many unconventional superconducting systems mentioned above suggests an unconventional magnetism-mediated paring mechanism. Its unconventional nature is also substantiated by the observations of strange-metal behavior in the normal-state resistance near P_c and an unusually large $\mu_0H_{c2}(0T)$ exceeding the Pauli limit. Since the theoretical calculations on KMn_6Bi_5 suggest dominant contributions of Mn-3d orbital electrons to the density of states at Fermi level, it becomes the first ternary Mn-based superconductor with a relatively high T_c of 9.3 K, which is one order of magnitude higher than that of MnP (~1 K). In contrast to the binary MnP, the flexibility of the crystal structure and chemical compositions in the ternary AMn_6Bi_5 (A = alkali metal) can open a new avenue for finding more Mn-based superconductors.

Reference

[1] Z. Y. Liu, Q. X. Dong, P. T. Yang, P. F. Shan, B. S. Wang, J. P. Sun, Z. L. Dun, Y. Uwatoko, G. F. Chen, X. L. Dong, Z. X. Zhao, and J.-G. Cheng, Phys. Rev. Lett. **128**, 187001 (2022).

Authors

Z. Y. Liu[a,b], Q. X. Dong[a,b], P. T. Yang[a,b], P. F. Shan[a,b], B. S. Wang[a,b], J. P. Sun[a,b], Z. L. Dun[a,b], Y. Uwatoko, G. F. Chen[a,b], X. L. Dong[a,b], Z. X. Zhao[a,b], and J.-G. Cheng[a,b]

[a]Chinese Academy of Sciences

[b]University of Chinese Academy of Sciences

Pressured-Induced Superconducting Phase with Large Upper Critical Field and Concomitant Enhancement of Antiferromagnetic Transition in $EuTe_2$

Uwatoko Group

The interplay between static magnetism and conduction electrons has been a core topic in modern condensed matter physics spanning a broad spectrum of interesting phenomena including the Kondo physics and heavy fermions, dilute magnetic semiconductors, giant/colossal magnetoresistance, and spintronics. Recently, the addition of nontrivial band topology to this topic leads to more exotic topological quantum phenomena such as quantum anomalous Hall effect and the intrinsic large anomalous Hall effect. When the conduction electrons condense into Cooper pairs and coexist with static magnetism in the magnetic superconductors, unconventional pairing states with intriguing superconducting properties can emerge as exemplified by the U- and Eu-based magnetic superconductors. Due to the antagonistic nature between magnetism and superconductivity, however, the magnetic superconductors are rare, and the concurrence of abovementioned phenomena in a single material is even scarce. Recently, we reported on a rare case that manifests an intimated interplay among static magnetism, conduction electrons, and possible exotic superconductivity through pressure regulations on an antiferromagnetic (AF) semiconductor $EuTe_2$ [1].

At ambient pressure (AP), $EuTe_2$ crystallizes in a $CuAl_2$-type tetragonal structure with space group I4/mcm. As seen in the inset of Fig. 1, each Eu^{2+} ion is surrounded by eight Te atoms, which form the $[Te_2]^{2-}$ dimers stacking along the c-axis. Upon cooling down at zero field, $EuTe_2$ exhibits a semiconducting behavior in resistivity and the Eu^{2+} moments develop a type-A AF order below $T_N = 11$ K, having the c-axis-oriented ferromagnetic (FM) Eu^{2+} layers coupled antiferromagnetically. When an external magnetic field is applied along c-axis, the type-A AF order can be tuned into a canted AF state through a spin-flop transition at $\mu_0H_1 = 2.3$ T and then a fully spin-polarized state at $\mu_0H_2 = 7.6$ T. Interestingly, these field-induced transitions have a profound impact on the transport properties of $EuTe_2$; i.e., ρ(T) under $\mu_0H > \mu_0H_1$ is altered from semiconducting to metallic-like behavior below a characteristic temperature $T_m >> T_N$, resulting in a large negative MR with over five orders of drop in resistivity at low temperatures. According to the density-

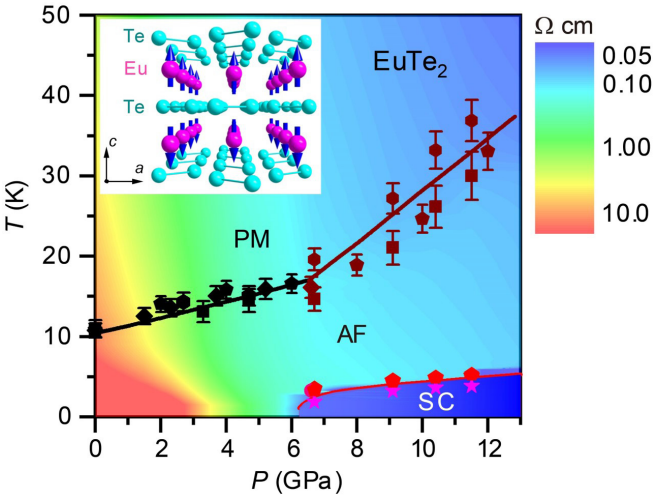

Fig. 1. Temperature-pressure phase diagram of $EuTe_2$. Inset shows the crystal and magnetic structures of $EuTe_2$ at ambient pressure.

functional-theory calculations, the charge carriers near the Fermi level originate mainly from the Te-5p orbitals and the small energy gap of $E_a \approx 16$ meV at zero field can be closed by lifting the band degeneracy of the Te-5p orbitals in the spin-flop state with a net FM component. This explains the field-induced metallic state and thus the large negative MR below T_m. These results thus demonstrated an intimated interplay between the static magnetism of Eu^{2+} sublattice and the charge carries from Te-5p orbitals in $EuTe_2$.

Considering the fact that many Te-containing materials become superconducting at ambient and/or high pressures, we are motived to pursue whether $EuTe_2$ can be driven into a magnetic superconductor upon compression. So, we investigate the effect of pressure on the transport and magnetic properties of $EuTe_2$ single crystals by using a cubic anvil cell apparatus. The main results are summarized in the temperature–pressure phase diagram of $EuTe_2$ in Fig. 1. We find that the application of high-pressure drives $EuTe_2$ from an AF semiconductor showing a large negative MR into a magnetic superconductor with a large upper critical field comparable to the Pauli paramagnetic limit. Interestingly, the emergence of superconductivity above the critical pressure of $P_c \approx 6$ GPa is accompanied with a concomitant enhancement of T_N, which experiences a quicker rise with the slope increased dramatically from $dT_N/dP = 0.85(14)$ K/GPa for $P \leq Pc$ to 3.7(2) K/GPa for $P \geq Pc$. Moreover, the superconductivity can survive in the spin-flop state with a net FM component of the Eu^{2+} sublattice under moderate fields $\mu_0 H \geq 2$ T, implying a possible exotic pairing state. Our findings establish the pressurized $EuTe_2$ as a rare magnetic superconductor, and these new results under high pressures have enriched the physics pertinent to the interplay between static magnetism and conduction electrons in this interesting compound.

Reference

[1] P. T. Yang, Z. Y. Liu, K. Y. Chen, X. L. Liu, X. Zhang, Z. H. Yu, H. Zhang, J. P. Sun, Y. Uwatoko, X. L. Dong, K. Jiang, J. P. Hu, Y. F. Guo, B. S. Wang, and J.-G. Cheng, Nature Commun. **13**, 2975 (2022)

Authors

P. T. Yang[a,b], Z. Y. Liu[a], K. Y. Chen[a,b], X. L. Liu[c], X. Zhang[c], Z. H. Yu[c], H. Zhang[a,b], J. P. Sun[a,b,d], Y. Uwatoko, X. L. Dong[a,b,d], K. Jiang[a,b,d], J. P. Hu[a,b], Y. F. Guo[c] B. S. Wang[a,b,d], and J.-G. Cheng[a,b]

[a]Chinese Academy of Sciences
[b]University of Chinese Academy of Sciences
[c]Shanghai Tech University
[d]Songshan Lake Materials Laboratory

Pressure Induced Superconductivity and Multiple Structural Transitions in CsCl-Type Cubic CeZn Single Crystal

Uwatoko Group

The CsCl-type compound crystallizing in cubic structure with chemical formula *ReTm* (where *Re* = rare earth elements such as La, Ce, Pr…etc., and *Tm* = typical metal elements such as Ag, Zn, Cd, …etc.) have been known for last three decades due to their strong correlation between charge, spin, and lattice degrees of freedom. These compounds undergo a cubic-to-tetragonal structural transition on cooling, followed by a magnetically ordered state at a lower temperature.

Among these, CeZn is distinct because the magnetic and structural transitions are coupled, revealing a first-order nature of the transition. CeZn exhibits antiferromagnetic (AFM) order below the Neel temperature, $T_N \sim 30$ K, and a concurrent crystal structural change from cubic to a tetragonal structure [1,2]. So far, the electrical, magnetic, and structural properties of CeZn have been investigated by substituting Cu in place of Zn, $CeZn_{1-x}Cu_x$ [3], and applying pressure up to 2.9 GPa [1]. On applying pressure, the AFM ordering changes to ferromagnetic (FM) ordering above 1 GPa, and the coupled magnetic and crystal structural transitions become separated. The neutron diffraction study [2] pointed that the crystal structure altered from cubic to rhombohedral structure in the FM state. With further increase in pressure, the Curie temperature, T_C, of the FM state was found to decrease with pressure, while the structural transition temperature increases and reaches room temperature around 3.0 GPa. However, further investigation of the lattice structure and electronic properties of CeZn at higher pressure has remained unexplored.

CeZn single crystals were synthesized by melting Ce and Zn with a 1:1 ratio as starting material in a tungsten crucible sealed inside a quartz tube under vacuum. Resistivity under high pressure was measured using a clamp type piston cylinder cell and a palm cubic anvil cell. The single crystal X-ray diffraction was carried out by using Rigaku XtaLab HyPix-6000 diffractometer with Mo-Kα radiation (λ = 0.71073 Å).

Figure 1 shows the temperature dependence of the electrical resistivity ρ of a CeZn single crystal at some

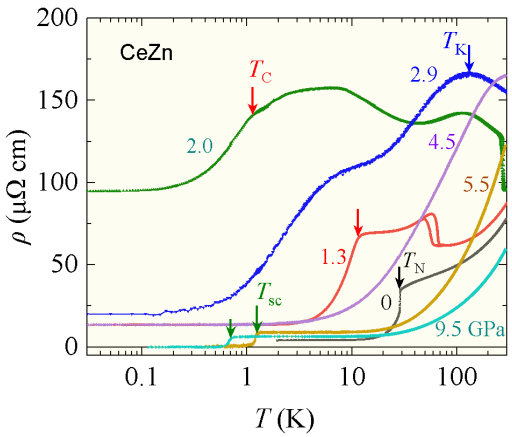

Fig. 1. Temperature dependence of electrical resistivity ρ, of CeZn single crystal at some selected pressures. Black and red arrows show the magnetic transition temperatures, T_N and T_C, respectively. Blue arrow indicates Kondo temperature (T_K), and green arrows indicate superconductivity transition temperature (T_{sc}).

selected pressures from 300 K down to 30 mK. At ambient pressure, ρ(T) monotonically decreases with temperature and drops suddenly below T_N = 29.0 K. It is clear from Fig. 1 that the coupled structural and magnetic transition become separated on increasing pressure above 1.0 GPa, in agreement with the earlier report [1,2]. At 1.3 GPa, the bend at the lower temperature side is assigned to the pressure-induced FM state, while the thermal hysteresis appearing at the high temperature side is attributed to the crystal structural transition. On increasing pressure to 2.0 GPa, FM state shifts towards lower temperature and the crystal structural transition temperature almost reaches to 280 K. Here, it is worthy to note that, in contrast to earlier result [1], in the present case, the crystal structural transition exceeds room temperature at lower pressure. This is clear by the absence of hysteretic behavior in ρ(T) below 300 K even at 2.9 GPa. This difference is attributed to the higher quality of sample used in the present study than the earlier polycrystalline samples [1]. Moreover, at 2.9 GPa, the signature of T_C disappears, and another big hump appears around 100 K, implying the pronounced Kondo effect. Up to 5.0 GPa, ρ(T) shows a normal metallic behavior in the measured temperature range. Surprisingly, on slightly increasing the pressure to 5.5 GPa as shown in Fig. 1, ρ(T) displays a pronounced drop below ~1.3 K and reaches zero around 0.8 K, signaling the occurrence of a superconducting state, which survives even up to 9.5 GPa.

To find the microscopic origin of these anomalies, we performed single crystal X-ray diffraction of CeZn at selected pressures at room temperature. From the X-ray diffraction analysis, we deduce that the crystal structure of CeZn sequentially evolves with increasing pressure from a cubic structure (at ambient pressure) to tetragonal (at 2.8 GPa), orthorhombic (at 4.2 GPa) and finally to monoclinic (at 8.2 GPa). To find a correlation between the crystal structure and the underlying electronic properties with increasing pressure, we have constructed a temperature (T)—pressure (P) phase diagram of CeZn, as shown in Fig. 2. The coupled magnetic transition, PM to AFM state,

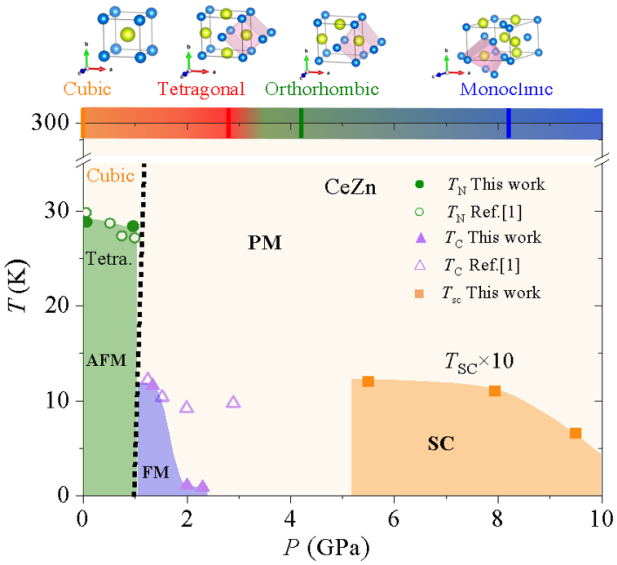

Fig. 2. Temperature–pressure phase diagram of CeZn. T_N, T_C, and T_{sc} are the Néel temperature, the Curie temperature and the superconducting transition temperature determined from the resistivity data, respectively. For clarity, T_{sc} has been multiplied by a factor of 10. The stars indicate the pressure value at which the single crystal X-ray diffraction measurements are performed. The tetragonal structure in the AFM region is obtained from Ref. [2]. The cubic to the tetragonal structure boundary line has been used from Ref. [1].

and the structural transition, cubic to tetragonal structure due to the magnetic striction, at T_N decreases hardly up to 1.0 GPa [1,2]. Above 1.0 GPa, the pressure induced an another cubic-to-tetragonal structural transition caused by the band Jahn-Teller effect [4]. The T–P phase diagram reveals that the electronic properties of CeZn also change simultaneously across the structural transitions. First, the ground state changes AFM to FM due to the cubic-to-tetragonal structural transition with pressure. T_C decreases rapidly to 1.1 K in the tetragonal structure as pressure increases to 2.0 GPa, implying a possible existence of a quantum critical point. Secondly, at the tetragonal-to-orthorhombic structural transition, CeZn transforms into a nonmagnetic simple metallic state. Finally, superconductivity emerges below T_{sc} ~ 1.3 K around 5.5 GPa possibly when the crystal structure changes from orthorhombic to monoclinic. The superconducting states survive up to 9.5 GPa in the monoclinic crystal structure. Here, it is worth noting that the T–P diagram of CeZn is different from that of the other Ce-based superconductors, in which superconductivity appears very close to the magnetic quantum critical point, whereas superconductivity in CeZn appears far away from the magnetic state. These results may suggest that the emergence of superconductivity in CeZn under pressure is related to the change in crystal structure implying a nonmagnetic origin of the Cooper pair formation.

In summary, we have performed systematic electrical resistivity and single crystal X-ray diffraction measurement of CeZn under high pressure up to 9.5 GPa. We find that CeZn exhibits multiple crystal structural transitions under pressure. Simultaneously, across these crystal structural transitions, the signature of modification of the underlying electronic properties of CeZn is also detected. Also, we would like to add that further investigation of how crystal structural change with decreasing temperature at a fixed pressure is required for detailed understanding about the relationship between the crystal structure and electronic properties.

References

[1] H. Kadomatsu, H. Tanaka, M. Kurisu, and H. Fujiwara, Phys. Rev. B **33**, 4799 (1986).
[2] T. Shigeoka, Y. Uwatoko, H. Fujii, L. Rebelsky, S. M. Shapiro, and K. Asai, Phys. Rev. B **42**, 8394 (1990).
[3] Y. Uwatoko, Y. Fujii, M. Nishi, K. Motoya, and Y. Ito, J. Magn. Magn. Mater. **76**, 411 (1988).
[4] H. Ihrig, D.T. Vigren, J.Kübler, and S. Methfessel, Phys. Rev. B **8**, 4525 (1973).

Authors
X. Shen[a], H. Ma, D. Bhoi, J. Gouchi, Y. Uwatoko, A. Dalan[b], Y. Kawamura[b], H. Sato[c], I. Umehara[a] , and M. Uehara[a]
[a]Yokohama National University
[b]Muroran Institute of Technology
[c]Rigaku Corporation, Akishima

Large Magnetic-Field-Induced Volume Change in Sintered Chromium Tellurides

Okamoto Group and X-Ray Diffraction Section

There is a long history in the study of magnetic-field-induced strains in ferromagnets. The most classical examples are iron and nickel, which show linear strains of several ppm to several tens of ppm by applying a magnetic field. The fact that their shapes can be changed by applying a magnetic field means that it can be used as an actuator that converts input energy or signal into mechanical movement. The small

magnetostrictions in iron and nickel are insufficient for this application, but in 1960s, giant magnetostrictive materials such as Terfenol-D, exhibiting a large strain exceeding 2000 ppm, have been developed and used as a material for magnetostrictive actuators. In such magnetostrictions in ferromagnetic metals, the volume change is small. In contrast, there are a few materials that exhibit a large volume change in magnetic fields (forced volume magnetostriction), such as invar alloys. Invar alloys exhibit very small thermal expansion over a wide temperature range due to the magnetovolume effect, which also plays an important role in the manifestation of the large volume change in magnetic fields.

We have discovered large magnetic-field-induced volume changes in Cr-based magnets such as $LiInCr_4S_8$ and $AgCrS_2$, which were hardly recognized as candidates for magnetostrictive materials [1,2]. Large volume increases reaching $\Delta V/V = 700$ ppm under a magnetic field of 9 T were observed in $LiInCr_4S_8$ just below the Néel temperature of $T_N = 24$ K and in $AgCrS_2$ at $T_N = 42$ K. Unlike invar alloys, these Cr-based magnets are antiferromagnetic insulators, suggesting that the large volume increases are caused by a complex interplay between the characteristic features of Cr spins, such as magnetic ordering accompanied by structural distortion, strong spin–lattice coupling, and geometrical frustration. However, the large volume changes were realized only at low temperature due to the low Néel temperatures, which is a disadvantage as a volume function. Therefore, we focused on Cr_3Te_4, which shows a ferromagnetic transition at a high temperature of $T_C = 330$ K. Cr_3Te_4 is ferromagnetic unlike the above Cr sulfides but is promising if the characteristic features of Cr-based magnets are utilized. In fact, we found that Cr_3Te_4 sintered samples, shown in the inset of Fig. 1(c), show magnetic-field-induced strains accompanied by large volume changes in a wide temperature region including room temperature [3].

Figure 1 shows the linear strains in magnetic fields of a Cr_3Te_4 sintered sample measured at various temperatures. The strains in Cr_3Te_4 can be understood as the summation of two components that are isotropic strain with the volume change and anisotropic strain with the shape change shown in Fig. 1(a). The latter shows small values up to several tens of ppm, which correspond to the ferromagnetic magnetization curve, suggesting that Cr_3Te_4 showed usual behavior as a ferromagnet. In contrast, as shown in Fig. 1(b), the volume changes in magnetic fields are very large reaching $\Delta V/V$

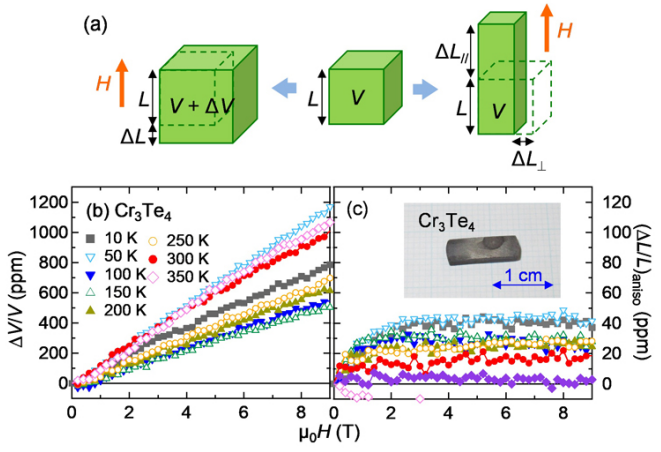

Fig. 1. (a) Isotropic (left) and anisotropic (right) magnetic-field-induced strains. (b) The volume changes in magnetic fields of a Cr_3Te_4 sintered sample measured at various temperatures. (c) The anisotropic strains in magnetic fields, corresponding to $\Delta L_\perp$ in the right panel of (a), of a Cr_3Te_4 sintered sample. The inset shows the Cr_3Te_4 sintered sample.

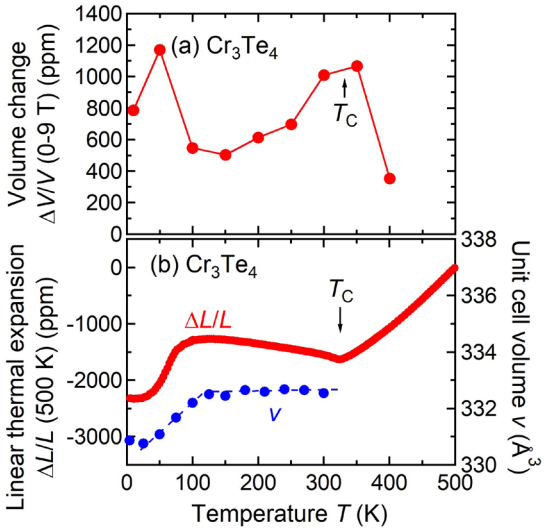

Fig. 2. (a) The volume changes of a Cr_3Te_4 sintered sample by applying a magnetic field of 9 T. (b) Linear thermal expansion with the reference temperature of 500 K (left) and unit cell volume determined by powder X-ray diffraction experiments (right) of a Cr_3Te_4 sintered sample.

=1200 ppm at a magnetic field of 9 T. This value is nearly twice as large as the maximum value of volume changes observed in Cr-based magnets as well as comparable to those of invar alloys. It is notable that a magnetic field of 9 T induced a significant volume change over 1000 ppm at room temperature and that the volume changes over 500 ppm throughout the entire temperature range below 350 K, as shown in Fig. 2(a).

The magnetic-field-induced volume changes in the Cr_3Te_4 sintered sample are particularly large near the Curie temperature, suggesting that the ferromagnetic order plays an essential role for the manifestation of the large volume increase. As shown in the linear thermal expansion shown in Fig. 2(b), a Cr_3Te_4 sintered sample showed a negative thermal expansion in a wide temperature range of 120–330 K below T_C, where the volume increases with decreasing temperature. This result indicates that Cr_3Te_4 gradually changes from paramagnetic to ferromagnetic ordered states with decreasing temperature, implying that the ferromagnetic order is enhanced by applying a magnetic field in this temperature region, resulting in the large magnetic-field-induced volume change.

The thermal expansion of the Cr_3Te_4 sintered sample has another feature that the volume change associated with the ferromagnetic order does not match the volume change of a unit cell. As seen in the Fig 1(b), there is no temperature region where the unit cell volume increases with decreasing temperature. This discrepancy suggests that the negative thermal expansion in the Cr_3Te_4 sintered sample is due to the "mictrostructural effects", discussed in β-eucryptite and Ca_2RuO_4, etc.[4,5] In Cr_3Te_4, the large magnetic-field-induced volume change and negative thermal expansion have the same origin that is the volume change at the ferromagnetic order, strongly suggesting that the microstructural effects play an important role in the emergence of the large magnetic-field-induced volume change. This is a different mechanism from the strong magnetovolume effect for invar alloys and might be a novel magneto-volume phenomenon occurring in Cr-based magnets.

References
[1] T. Kanematsu, M. Mori, Y. Okamoto, T. Yajima, and K. Takenaka, J. Phys. Soc. Jpn. **89**, 073708 (2020).
[2] T. Kanematsu, Y. Okamoto, and K. Takenaka, Appl. Phys. Lett. **118**, 142404 (2021).
[3] Y. Kubota, Y. Okamoto, T. Kanematsu, T. Yajima, D. Hirai, and K. Takenaka, Appl. Phys. Lett. **122**, 042404 (2023).
[4] F. H. Gillery and E. A. Bush, J. Am. Ceram. Soc. **42**, 175 (1959).
[5] K. Takenaka, Y. Okamoto, T. Shinoda, N. Katayama, and Y. Sakai, Nat. Commun. **8**, 14102 (2017).

Authors
Y. Okamoto, Y. Kubota[a], T. Kanematsu[a], T. Yajima, D. Hirai[a], and K. Takenaka[a]
[a]Nagoya University

Rotations of Methane Molecules in Amorphous and Crystalline Hydrates

Yamamuro Group

Methane hydrate has been studied extensively not only as a future energy resource but also from the interest in quantum and classical rotations of methane molecules. The crystalline methane hydrate (c-MH) forms a host water lattice of type I with two dodecahedral (12-hedral) and six tetradecahedral (14-hedral) cages per unit cell (space group: $Pm3n$), and each cage contains one methane molecule [1]. The chemical formula of c-MH is $CH_4 \cdot 5.75H_2O$. The "amorphous" MH (a-MH) was first prepared with a vapor-deposition method by our group [2]. The radial distribution functions derived from the neutron diffraction data demonstrated that the methane molecules are accommodated in the cage-like spaces even in amorphous structures. It is also known that the a-MH crystallizes into the c-MH around 175 K [3].

In this study, we have investigated the rotations of methane molecules in a-MH and c-MH. Our main interest is how the rotation of methane molecules is affected by the cage (like) structure, e.g., size and symmetry. The a-MH was prepared by depositing the mixture of CH_4 and D_2O gases onto the substrate cooled at 5 K using a custom-made cryostat [4], and c-MH was obtained by annealing the sample at 170 K under 0.1 MPa of CH_4 gas. Their quasi-elastic neutron scattering (QENS) and inelastic neutron scattering (INS) data were collected at 5 to 80 K using AGNES spectrometer at JRR-3, Tokai, Japan.

Figure 1 shows clear QENS broadening due to the

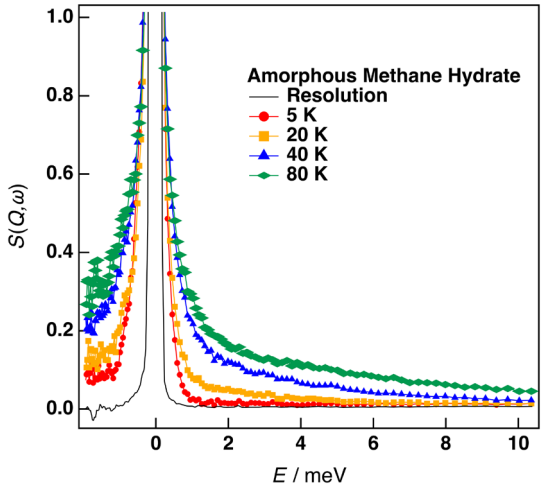

Fig. 1. Quasielastic neutron scattering spectra of amorphous methane hydrate. The data from all detectors are summed up. The average Q value is about 1.7 Å^{-1}.

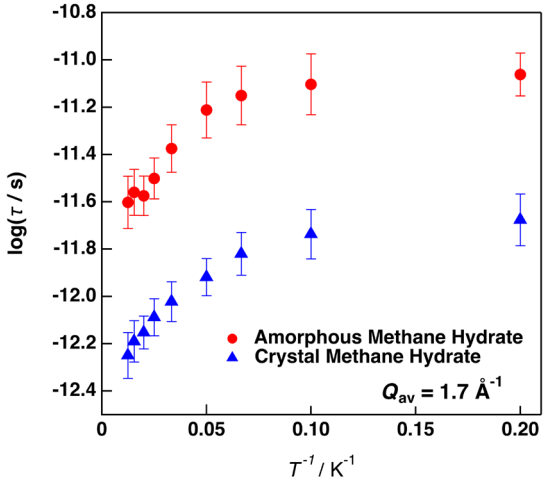

Fig. 2. Arrhenius plots of the relaxation times at Q_{av} = 1.7 Å^{-1} for the CH_4 rotation in amorphous and crystalline hydrates.

rotational motion of CH_4 accommodated in a-MH. It is worth noting that the QENS appeared even at 5 K. The data were well fitted to the combination of Delta and Lorentz functions as usual and the relaxation time τ was calculated from the peak width of the Lorentz function. Similar QENS data were observed also in c-MH. Figure 2 shows the Arrhenius plots for both a-MH and c-MH. There is a clear bending of the τ line around 20 K for both samples and the slope (activation energy ΔE_a) on the low-temperature side is very small (ΔE_a < 0.2 kJ/mol). We guess that there is a crossover between the classical (high-T) and quantum (low-T) rotations around 20 K; there is no temperature dependence of τ in a pure tunneling process. The a-MH has longer τ than that of c-MH. This is probably because the cage space in a-MH is narrower than that of c-MH. Additional neutron diffraction and calorimetric experiments are now going on to explain the QENS data more quantitatively.

References
[1] D. W. Davidson *et al*., Nature **311**, 142 (1984).
[2] T. Kikuchi *et al*., J. Phys. Soc. Jpn. **81**, 094604 (2012).
[3] M. Z. Faizullin *et al*., Chem. Eng. Sci. **130**, 135 (2015).
[4] O. Yamamuro *et al*., J. Chem. Phys. **115**, 9808 (2001).

Authors
M. Zhang, H. Akiba, and O. Yamamuro

Spin Excitation in a Chiral-Polar-Corundum Compound Ni_2InSbO_6

Masuda Group

In some types of non-centrosymmetric magnets, spin moments are incommensurately arranged to balance Dzyaloshinskii–Moriya (DM) and Heisenberg interactions.

This leads to helimagnetic spin textures and spin soliton lattice which exhibit distinctive magnetoelectric response and promising potential for applications in spintronics. A chiral-polar-corundum compound Ni_2InSbO_6 is an example for a proper-screw type spin structure realized by chirality-induced DM interaction [1], as shown in Fig. 1(a). In conventional helimagnets, a spin soliton lattice is induced in the magnetic field applied in the spin rotation plane. In contrast in Ni_2InSbO_6, the soliton lattice was proposed by a unique scenario. Suppose that additional DM interac-

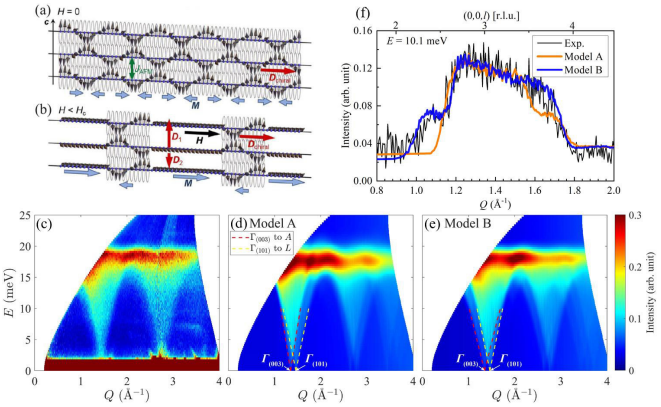

Fig. 1 Schematic of (a) proper-screw type helical spin structure and (b) spin soliton lattice in Ni_2InSbO_6. The figures were adopted from Ref. [1]. (c) INS spectrum measured with E_i = 30.5 meV at T = 10 K. (d),(e) Powder averaged LSWT calculation of INS spectra using the best fit parameters for model A in (d) and model B in (e). Modes of spin wave excitation from $\Gamma_{(003)}$ to $A_{(00\ 3/2)}$ and from $\Gamma_{(101)}$ to $L_{(1/2\ 0\ 1/2)}$ points are described by red and yellow dashed lines, respectively. (f) 1D-cut of powder spectrum at E = 10.1 meV for experiment (black), model A (orange) and model B (blue).

tions with the staggered vector component $\boldsymbol{D}_1$ and $\boldsymbol{D}_2$ along the polar c axis are assumed, as shown in Fig. 1(b). At zero magnetic field, localized magnetization components M are induced by $\boldsymbol{D}_1$ and $\boldsymbol{D}_2$ interacting between neighboring Ni^{2+} ions along the c axis, indicated by the light blue arrows in Fig. 1(a). In the magnetic field applied perpendicular to the spin rotation plane, they shrink or expand to minimize Zeeman energy, and hence the spin soliton lattice is realized. In previous Raman study [2], however, the spectrum was analyzed by the spin model assuming that the first and second neighbor Heisenberg interactions J_1 and J_2 were equal, corresponding that $\boldsymbol{D}_1$ and $\boldsymbol{D}_2$ were equal. The assumption was contradictory to the scenario based on the staggered DM vectors. Thus, in this work, we collected magnetic spectrum in wide momentum-energy space on Ni_2InSbO_6 by inelastic neutron scattering (INS) technique to identify the precise spin Hamiltonian and validate the mechanism of the spin soliton lattice [3].

The INS powder spectrum is shown in Fig. 1(c). Well-defined spin wave excitation is observed with the band energy of 20 meV at 10 K. Two spin models of antiferromagnetic Heisenberg Hamiltonian considering the first to fourth nearest neighbor interactions J_1 to J_4 are used to analyze the spectrum by the linear spin-wave theory (LSWT). The calculated spectra of model A with constraints $J_1 = J_2$ and $J_3 = J_4$ according to the previous Raman study [2] and model B without the constraints according to the crystallographic consideration are shown in Figs. 1(d) and 1(e), respectively. χ^2 and correlation coefficient R for model A were 8.8 and 0.928, and those for model B are 6.1 and 0.953, meaning that model B is more probable. Indeed, one-dimensional cuts of the experiment and calculations at the energy of 10.1 meV in Fig. 1(f) suggest that the model B reproduces the experiment better. The difference is, in fact, caused by the fast and low spin wave velocities along the c axis for model A and B, respectively. The spin model of Ni_2InSbO_6, thus, turns out to be a coupled two-dimensional lattice stacked along the c axis with intraplane interaction J_1 = 6.05 meV and interplane interaction J_1 = 0.95 meV. Since DM interaction is proportional to the corresponding exchange interaction, $\boldsymbol{D}_1$ and $\boldsymbol{D}_2$ are different as well, which validates the mechanism of spin soliton lattice [1].

References

[1] Y. Araki, T. Sato, Y. Fujima, N. Abe, M. Tokunaga, S. Kimura, D. Morikawa, V. Ukleev, Y. Yamasaki, C. Tabata, H. Nakao, Y. Murakami, H. Sagayama, K. Ohishi, Y. Tokunaga, and T. Arima, Phys. Rev. B **102**, 054409 (2020).

[2] M. A. Prosnikov, A. N. Smirnov, V. Y. Davydov, Y. Araki, T. Arima, and R. V. Pisarev, Phys. Rev. B **100**,144417 (2019).

[3] Z. Liu, Y. Araki, T. Arima, S. Itoh, S. Asai, and T. Masuda, Phys. Rev. B **107**, 064428 (2023).

Authors

Z. Liu, Y. Araki[a], T. Arima[a], S. Itoh[b,c], S. Asai, and T. Masuda

[a]The University of Tokyo

[b]Institute of Materials Structure Science, High Energy Accelerator Research Organization

[c]J-PARC Center

Spin Dynamics in Equilateral Triangular Spin Tube Material $CsCrF_4$

Masuda Group

Frustrated magnetism has attracted significant attention due to their potential to exhibit unique magnetic phases resulting from the competition between various interactions. Lattices composed of triangles as basic units, such as the triangular lattice, Kagome lattice, and Pyrochlore lattice, serve as representative examples of frustrated magnet systems. Triangular spin tube has been extensively studied theoretically as a one-dimensional frustrated system, where triangles are arranged in a single direction. In the Heisenberg equilateral triangular spin tube system, the spin correlation decays exponentially, and the ground state is a dimerized nonmagnetic state with a spin gap [1]. Furthermore, the presence of a Tomonaga-Luttinger liquid with chiral order has been predicted under the influence of anisotropy and a magnetic field [2].

In real materials, the presence of intertube interactions, albeit small, leads to the emergence of various magnetically ordered states [3]. As shown in Fig. 1(a), $CsCrF_4$ consists of Cr^{3+} ions forming equilateral triangular spin tubes with S = 3/2 spins. Magnetic susceptibility and heat capacity measurements did not exhibit any sign of phase transitions [4]. Nevertheless, neutron diffraction experiments unveiled the presence of a long-range order characterized by a 120-degree structure, along with successive phase transitions

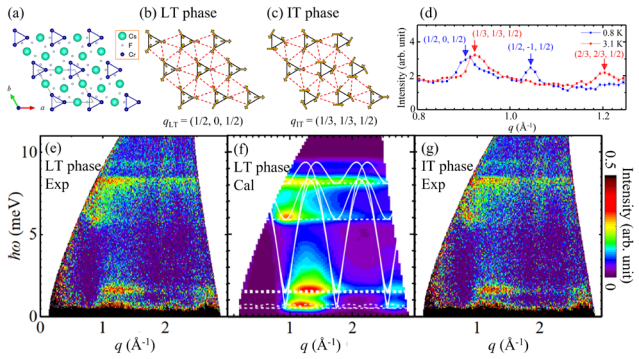

Fig. 1.(a) Crystal structure of $CsCrF_4$. Cr ions form equilateral triangular spin tubes with S = 3/2 spins along the crystallographic c axis. (b) Magnetic structure of $CsCrF_4$ in the LT phase. (c) Magnetic structure of $CsCrF_4$ in the IT phase. (d) Elastic part of INS spectra measured with E_i = 3.1 meV. (e) INS spectra measured with E_i = 15.3 meV at 0.8 K (LT phase). (f) Powder averaged INS spectra in LT phase calculated by linear spin-wave theory. The white solid and dashed curves are dispersion relations calculated along the c* and a* axes, respectively. (g) INS spectra measured with E_i = 15.3 meV at 3.1 K (IT phase).

where the propagation vector changes from q_{LT} in Fig. 1(b) to q_{IT} in Fig. 1(c) [5]. So far, the spin dynamics of this material have remained unexplored. In the present research, inelastic neutron scattering (INS) experiments were conducted using powder samples to determine the spin Hamiltonian and shed light on the successive phase transitions.

The experiment was conducted using the HRC spectrometer installed at J-PARC/MLF [6]. As shown in Fig. 1(d), magnetic Bragg peaks with q_{LT} were observed at 0.8 K and those with q_{IT} were observed at 3.1 K in the elastic part of the neutron spectra [5]. The observed and calculated INS spectra in the LT phase are shown in Figs. 1(e) and 1(f), respectively. For the latter, we used linear spin-wave theory on the basis of Heisenberg model of a triangular spin tube, including small DM interaction and a small single-ion anisotropy. The experiment was reasonably reproduced by the calculation. The spectrum in wide-energy range is explained by the quasi-one-dimensional nature of the spin tube in the c^* direction. The analysis highlighted the significant roles of the DM interaction and single-ion anisotropy in low-energy range.

Furthermore, as depicted in Fig. 1(g), the INS spectrum in the IT phase was measured. Surprisingly, despite the change in the propagation vector in the diffraction profiles in Fig. 1(d), the INS spectrum in the IT phase exhibited a striking resemblance to the LT phase in level of powder-averaged spectra. The same analysis method utilized for the LT phase was applied to analyze the INS spectrum in the IT phase. However, the INS spectra in the IT phase could not be reproduced, indicating that the successive phase transition is not driven by variations in the spin Hamiltonian parameters.

To gain further insights, a phase diagram of the ground state was calculated for the coupled spin tubes system. The parameter values of the spin Hamiltonian estimated by the present INS experiment lie near the boundary between the magnetic phases with the structures of q_{IT} and q_{LT}. This finding implies that the internal energy of the magnetic structures in the LT and IT phases is similar. Considering that large spin entropy can favor the selection of the magnetic structure, it is proposed that the gain in spin entropy serves as the origin of the successive phase transition. Notably, this study provides the first evidence that, despite disparities in the static structures, the dynamic structures exhibit similarity under such circumstances.

References

[1] K. Kawano, and M. Takahashi, J. Phys. Soc. Jpn. **66**, 4001 (1997).
[2] T. Sakai, M. Sato, K. Okunishi, Y. Otsuka, K. Okamoto, and C. Itoi, Phys. Rev. B **78**, 184415 (2008).
[3] K. Seki and K. Okunishi, Phys. Rev. B **91**, 224403 (2015).
[4] H. Manaka, Y. Hirai, Y. Hachigo, M. Mitsunaga, M. Ito, and N. Terada, J. Phys. Soc. Jpn. **78**, 093701 (2009).
[5] M. Hagihala, S. Hayashida, M. Avdeev, H. Manaka, H. Kikuchi, and T. Masuda, npj Quantum Mater. **4**, 14 (2019).
[6] H. Kikuchi, S. Asai, H. Manaka, M. Hagihala, S. Itoh, and T. Masuda, Phys. Rev. B **107**, 184404 (2023).

Authors

H. Kikuchi, S. Asai, H. Manaka[a], M. Hagihala[b], S. Itoh[b], and T. Masuda

[a]Kagoshima University

[b]Institute of Materials Structure Science, High Energy Accelerator Research Organization

Spin Fluctuations in Spin-Hedgehog-Anti-Hedgehog Lattice State in $MnSi_{1-x}Ge_x$

Nakajima Group

Couplings between topological magnetic orders and conduction electrons have been of increasing interest in recent condensed matter physics research [1,2]. One of the most well-known examples is the magnetic skyrmion lattice (SkL) discovered in a chiral cubic helimagnet MnSi [1]. The SkL is composed of topologically-nontrivial vortex like spin objects, which have finite scalar spin chirality, $S_i \cdot (S_j \times S_k)$, owing to the non-coplanar arrangements of the magnetic moments. The scalar spin chirality acts as an effective magnetic field for conduction electrons, and thus induces an unconventional Hall effect, which is known as Topological Hall Effect (THE). Another example of topological magnetic orders is a spin-hedgehog-anti-hedgehog (SHAH) lattice state discovered in MnGe [3], which is isostructural to MnSi. The spin arrangement of SHAH lattice is described by a superposition of three proper-screw-type magnetic modulations with the q-vectors of $(q,0,0)$, $(0,q,0)$ and $(0,0,q)$. By calculating spatial distribution of the scalar spin chirality in the SHAH lattice, one can find that the spin texture can be viewed as periodic arrays of effective magnetic monopoles and antimonopoles. Although the effective magnetic fields in the SHAH lattice are cancelled to be zero in zero magnetic field, an application of an external magnetic fields and resulting distortion of the SHAH lattice can induce a finite THE. In addition to the THE mechanism for the long-range-ordered non-coplanar magnetic orders, a recent theoretical study [4] has pointed out that 'fluctuating' short range magnetic order with scalar spin chirality can induce skew scattering, which leads to Hall effect with opposite sign to that induced by the long-range non-coplanar orders.

In the present study, we investigate $MnSi_{1-x}Ge_x$, which exhibits a variety of Hall effects depending on temperature, magnetic field, and amount of the chemical substitution [5]. Specifically, we focus on $x = 0.8$ and 0.6 samples; the former exhibits the same SHAH lattice state as that in the $x = 1$ sample, while the latter shows another SHAH lattice state composed of four q-vectors, specifically (q,q,q), $(q,-q,-q)$, $(-q,q,-q)$ and $(-q,-q,q)$ [5]. To understand the origins of the Hall effects in these systems, it is necessary to experimen-

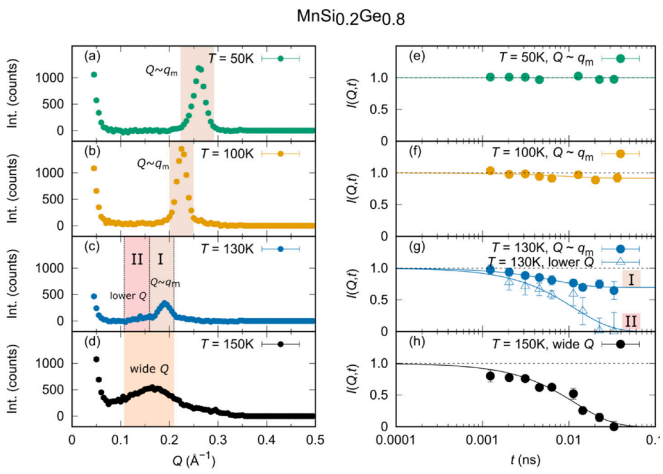

Fig. 1. (a)–(d) Q-dependence of intensity in the $x = 0.8$ sample measured at four representative temperatures. (e)–(h) Intermediate scattering function of $I(Q,t)$ deduced from the selected Q-range given in (a)–(d).

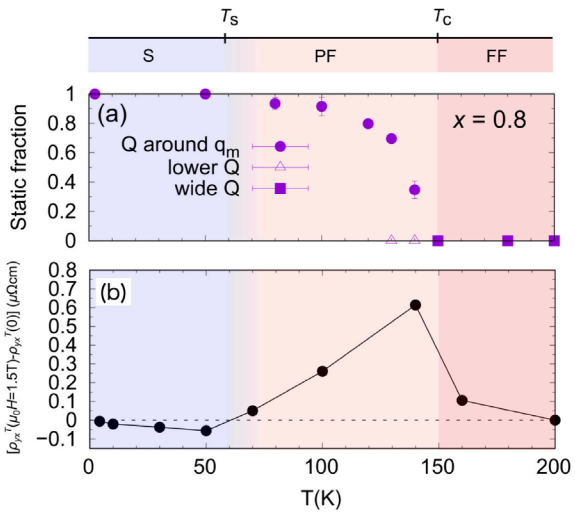

Fig. 2. Temperature dependence of (a) the volume fraction of the static spin component and (b) the topological Hall resistivity at $\mu_0 H$ = 1.5 T, measured in the x = 0.8 sample.

tally study the magnetic structures and their fluctuations by neutron scattering.

Figure 1 shows the results of the neutron scattering measurements on the x = 0.8 sample. The data was obtained at VIN ROSE (BL06) beamline in Materials and Life-science experimental Facility (MLF) of J-PARC. We used the powder sample of $MnSi_{1-x}Ge_x$ with x = 0.8 used in the previous study in Ref. 5. Figures 1(a)–1(d) show the neutron diffraction profiles in the low-Q region. At low temperatures, a sharp magnetic Bragg peak was observed at around Q = 0.26 Å^{-1}. As the temperature was increased, the intensity of the Bragg peak was reduced, and its position was shifted toward lower Q region. Finally, the Bragg peak disappeared above the critical temperature of 150 K, and instead, a broad diffuse scattering was observed at around Q = 0.15 Å^{-1}.

Figures 1(e)–1(h) show the intermediate correlation function $I(Q,t)$ deduced from the neutron resonance spin echo spectroscopy at VIN ROSE. The Q ranges used for the data reduction are indicated by colored area in Figs. 1(a)–1(d). At 50 K, the $I(Q,t)$ remains very close to unity even at 0.03 ns, which is the upper limit of the time window of the present experiment, indicating that there is no spin fluctuations and that the magnetic moments are static. However, near the critical temperature, we observed the $I(Q,t)$ curve shows the exponential decay, meaning that the spins are fluctuating with the characteristic time of approximately 0.01 ns. In Fig. 2(a), we show the fraction of the fluctuating spin components deduced form the neutron spin echo experiment as function of temperature, revealing that the spin fluctuations remain above 60 K. This shows a good agreement with the sign change of the additional Hall resistivity shown in Fig. 2(b); the additional component of the Hall resistivity changes from negative to positive at around 60 K. These observations demonstrated that the dominant contribution of the additional Hall resistivity changes from the static emergent magnetic field from the long-range-ordered SHAH lattice to the skew scattering due to the fluctuating spin cluster with scalar spin chirality as the temperature is increased. We also performed the neutron spin echo measurements on the x = 0.6 sample in the same manner as that for the x = 0.8 sample, and carried out inelastic neutron scattering experiments for both the x = 0.6 and 0.8 samples at HRC (BL12) in MLF of J-PARC. More detailed analysis will be published elsewhere [6].

References

[1] S. Muhlbauer *et al.*, Science **323**, 915 (2009).
[2] N. Nagaosa and Y. Tokura, Nat. Nanotech. **8**, 899 (2013).
[3] N. Kanazawa *et al.*, Phys. Rev. Lett. **106**, 156603 (2011).
[4] H. Ishizuka and N. Nagaosa, Sci. Adv. **4**, eaap9962 (2018).
[5] Y. Fujishiro *et al.*, Nat. Commun. **10**, 1059 (2019).
[6] S. Aji *et al.*, arXiv:2305.01172

Authors

S. Aji[a], T. Oda[a], Y. Fujishiro[b], N. Kanazawa[a], H. Saito[a], H. Endo[c], M. Hino[d], S. Itoh[c], T. Arima[a,b], Y. Tokura[a,b], and T. Nakajima[a,b]
[a]University of Tokyo
[b]RIKEN Center for Emergent Matter Science
[c]KEK
[d]Kyoto University

Quasi-Elastic Neutron Scattering Study on Stretched Polymer Gels

Mayumi Group

Hydrogels, cross-linked polymer networks containing water, are expected to be applied for biomaterials and the mechanical toughness of polymer gels needs to be improved. The reason for the brittleness of polymer gels is the heterogeneous strain distribution caused by their inhomogeneous network structure. When a polymer gel is stretched, local stress concentrates on at short strands between cross-links. The stress-concentrated strands are highly stretched and become potential fracture onsets, which dominates the macroscopic fracture properties of polymer gels.

In this study, the segment/monomer dynamics of polymer

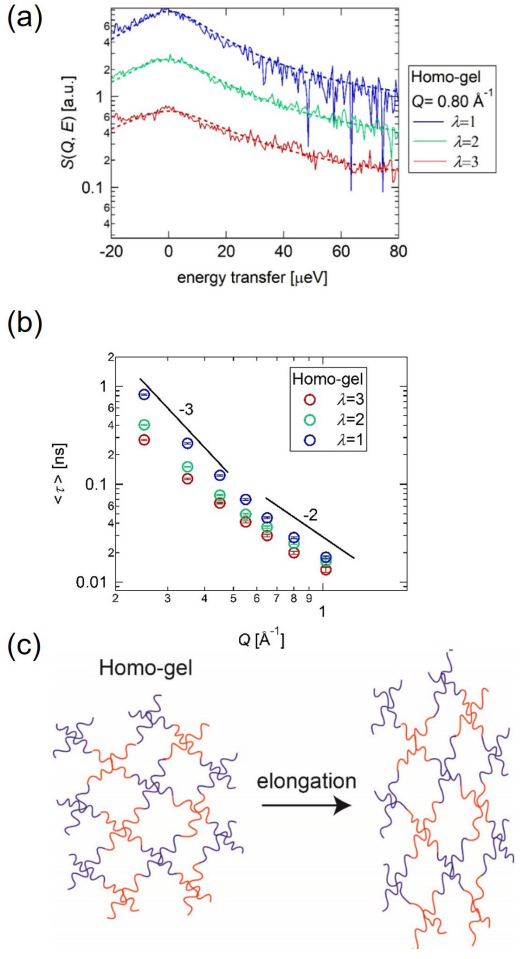

Fig. 1 (a) Dynamic structure factor $S(Q, \omega)$ of Homo-gel at λ =1, 2, 3, (b) Q dependence of average relaxation time for Homo-gel at λ =1, 2, 3, (c) Schematic illustration of deformation mechanism for Homo-gel.

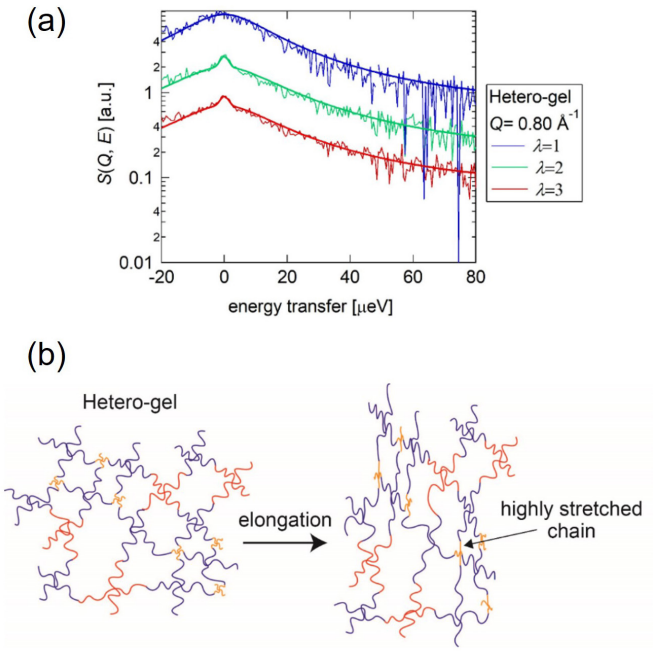

Fig. 2 (a) Dynamic structure factor $S(Q, \omega)$ of Hetero-gel at λ =1, 2, 3, (b) Schematic illustration of deformation mechanism for Hetero-gel.

gels under uniaxial deformation is investigated by means of quasi-elastic neutron scattering (QENS) [1]. In order to clarify the effect of heterogeneity in polymer network structure, we prepared two types of polymer gels with controlled heterogeneities: a homogeneous Tetra-PEG gel prepared by end-cross-linking of Tetra-arm prepolymers (Homo-gel) [2], and heterogeneous Tetra-PEG gel (Hetero-gel) containing a small amount of Tetra-PEG prepolymers with shorter arms [3]. Hetero-gel shows a more brittle fracture behavior than Homo-gel, which suggests a stress-concentration occurs in Hetero-gel under deformation.

Figures 1 (a) shows $S(Q, \omega)$ for Homo-gel under uniaxial deformation (λ = 1, 2, 3) at Q = 0.8 Å^{-1}. The dynamic structure factors were fitted with a KWW function. As shown in Figure 1 (b), the average relaxation times (τ) of Homo-gel decrease with increasing stretching, and the segment/monomer dynamics in the gel are accelerated by stretching. Stretching exponent β for the homogeneous gel is not changed with stretching, suggesting that the local deformation in the gel is kept homogeneous (Fig. 1 (c)).

Figures 2 (a) shows $S(Q, \omega)$ of Hetero-gel under uniaxial deformation (λ = 1, 2, 3) at Q = 0.8 Å^{-1}. A sharp elastic peak corresponding to slow chain dynamics with a broad base was observed under deformation (λ = 2, 3), while only a broad peak was seen for the un-deformed state (λ =1). This means that the slow chain dynamics appears only for the deformed Hetero-gel. The elastic component can be ascribed to a slow chain dynamics of highly stretched short strands (Fig. 2 (b)). When Hetero-gel is stretched, the short strands oriented to the stretching direction are strongly stretched and the chain dynamics of the highly deformed chains is suppressed, which causes a more brittle macroscopic fracture compared with that in the case of Homo-gel.

References

[1] K. Aomura, Y. Yasuda, T. Yamada, T. Sakai, and K. Mayumi, Soft Matter, **19**, 147 (2023).

[2] T. Sakai, T. Matsunaga, Y. Yamamoto, C. Ito, R. Yoshida, S. Suzuki, N. Sasaki, M. Shibayama, and U. I. Chung, Macromolecules **41**, 5379 (2008).

[3] S. Kondo, H. Sakurai, U. I. Chung, and T. Sakai, Macromolecules **46**, 7027 (2013).

Authors

K. Aomura, Y. Yasuda[a], T. Yamada[b], T. Sakai[a], and K. Mayumi

[a]The University of Tokyo

[b]Neutron Science and Technology Center, Comprehensive Research Organization for Science and Society (CROSS)

Detection of the Spatial Modulation of the FFLO State in High Magnetic Fields

Kindo and Kohama Groups

Superconductivity appears as a result of forming pairs of itinerant electrons by an attractive force. In the case of conventional superconductivity, the electron pairs are composed of electrons with momenta $\boldsymbol{k}$ and $-\boldsymbol{k}$. In 1964, Fulde & Ferrell [1] and Larkin & Ovchinnikov [2] proposed that an imbalanced pairing of up-/down-spin electrons with momenta $\boldsymbol{k}$ and $-\boldsymbol{k}+\boldsymbol{q}$, known as the FFLO state, can be realized in high fields where Zeeman splitting energy exceeds the superconducting energy gap. In the FFLO state, the finite total momentum of the pair $\boldsymbol{q}$ modifies the order parameter of the superconductivity and yields the term $\cos(\boldsymbol{qr})$, which results in spatial oscillations of the superconductivity in real space. Although the spatial modulation of the order parameter is one of the most decisive pieces of evidence of the FFLO state, it has never been experimentally observed.

In order to detect the spatial modulation, we carried out multi-directional ultrasound measurements of one of the FFLO candidates, an organic superconductor κ-(BEDT-TTF)$_2$Cu(NCS)$_2$, in pulsed magnetic fields [3]. Figure 1 shows the magnetic-field dependence of sound velocity at 1.6 K when polarization vectors of sound waves $\boldsymbol{u}$ are along the crystal axes parallel to the conducting plane, b and c. Magnetic fields are applied parallel to the c axis. From the results of previous studies of this material, the field where the Zeeman energy reaches the superconducting energy gap is expected to be about 21 T, and also, the superconductivity is completely suppressed above 25 T. Namely, the FFLO state can be stable in the field range of 21–25 T. Indeed, as clearly seen from

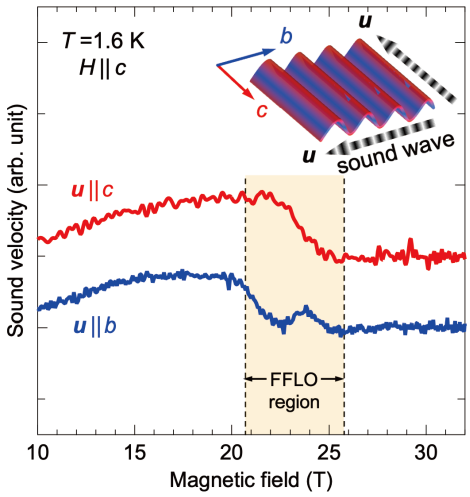

Fig. 1. Anisotropic acoustic response in the FFLO state.Magnetic field dependence of sound velocity at 1.6 K for $\boldsymbol{u}||b$ (blue) and $\boldsymbol{u}||c$ (red) in a magnetic field along the c axis. Only in the FFLO region between 21–25 T, the sound-wave-direction-dependent response is observed. The schematics in the inset show the spatial modulation of the FFLO state composed of superconductivity (red) and normal state (blue). The striped arrows signify the sound-wave directions, which are parallel to the polarization vector $\boldsymbol{u}$.

our results, only in this field region, a distinct difference appears between the two datasets. It is natural because the spatial modulation produced by the ***q*** vector, as shown in the inset of Fig. 1, must make the superconducting state anisotropic. Since only the ***u***||*b* data shows the enhancement of the sound velocity, the emergent superlattice of the spatial modulation should be parallel to the *b* axis. This means that ***q*** should orient along the *b* axis. In the case of κ-(BEDT-TTF)$_2$Cu(NCS)$_2$, it is expected that antiferromagnetic spin fluctuations along some nesting vectors mediate the pairing of the superconductivity, and one of the most predominant nesting direction points towards the ***b*** axis. It seems reasonable because an energy gain by better nesting stabilizes the FFLO state in a low-dimensional superconducting state. This agreement experimentally unveil the nature of the FFLO state occurred in the low-dimensional superconductivity.

Nowadays the concept of the unique pairing of the FFLO state has been widely investigated in various physics not only condensed matter physics but also elemental particle physics and so on. The present results demonstrate that the spatial modulation of the FFLO state can be discussed by the emergent anisotropy of the acoustic properties. Our findings will facilitate a deeper understanding of the FFLO state.

References

[1] P. Fulde and R. A. Ferrell, Phys. Rev. **35**, A550 (1964).
[2] A. I. Larkin and Y. N. Ovchinnikov, Zh. Eksp. Teor. Fiz. **47**, 1136 (1964).
[3] S. Imajo, T. Nomura, Y. Kohama, and K. Kindo, Nat. Commun. **13**, 5590 (2022).

Authors

S. Imajo, T. Nomura, Y. Kohama, and K. Kindo

Signature of Spin-Triplet Exciton Condensations in $LaCoO_3$ at Ultrahigh Magnetic Fields up to 600 T

Y. H. Matsuda Group

Bose–Einstein condensation of electron-hole pairs, exciton condensation, has been effortfully investigated since predicted 60 years ago. Irrefutable evidence has still been lacking due to experimental difficulties in verifying the condensation of the charge-neutral and non-magnetic spin-singlet excitons. On the other hand, condensation of spin-triplet excitons is a promising frontier because spin supercurrent and spin-Seebeck effects will be observable. A canonical cobaltite $LaCoO_3$ under very high magnetic fields is a propitious candidate, yet to be verified. In this study, we unveil the exotic phase diagram of $LaCoO_3$ up to 600 T generated using the electromagnetic flux compression method and the state-of-the-art magnetostriction gauge. We found continuous magnetostriction curves and a bending structure, which suggest the emergence of two distinct spin-triplet exciton condensates. By constructing a phenomenological model, we showed that quantum fluctuations of excitons are crucial for the field-induced successive transitions. The spin-triplet exciton condensation in a cobaltite, which is three-dimensional and thermally equilibrated, opens a novel venue for spintronics technologies with spin-supercurrent such as a spin Josephson junction.

$LaCoO_3$ has been claimed to be a promising candidate when placed under very high magnetic fields exceeding

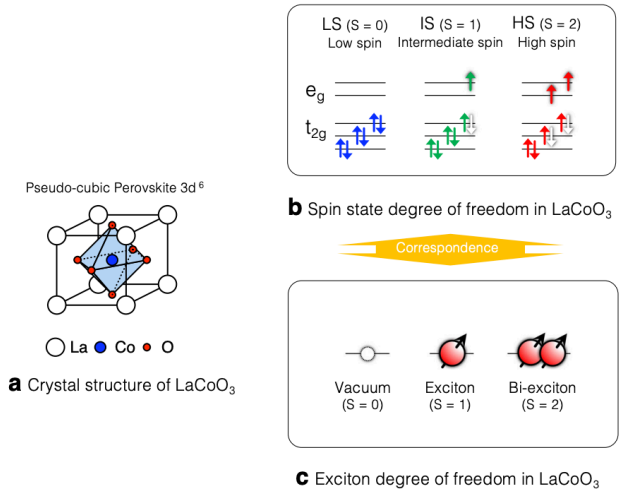

Fig. 1. Schematic illustrations describing the correspondence between spin-states and exciton states in $LaCoO_3$.

100 T. $LaCoO_3$ is an archetypal compound having a variety of spin-states, such as low-spin (LS: S = 0), intermediate spin (IS: S = 1) and high spin (HS: S = 2) states (See Fig. 1), which are viewed as vacuum, an exciton, and bi-exciton states, respectively (See Fig. 1). The spin-triplet exciton condensation will emerge when the magnetic field eliminates the spin-gap and changes the vacuum state (LS) to a magnetic exciton state (IS) or bi-exciton state (HS).

Previously in $LaCoO_3$, the field-induced phase transitions are uncovered below 30 K (α phase) and above 30 K (β phase), which extend beyond 100 T, using magnetization [1] and magnetostriction measurements [2] up to 200 T generated by single turn coil (STC) method. The two phases are considered superlattice formation (i.e., solidification) of the excitons, bi-excitons, and vacuum based on the observa-

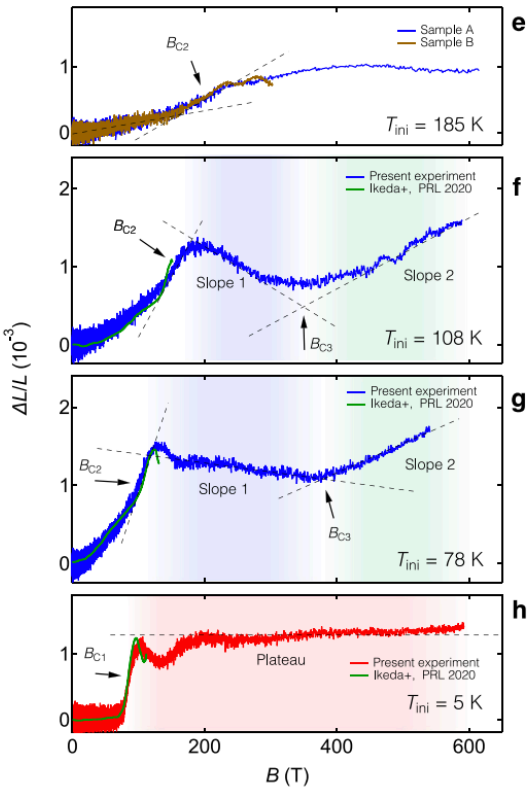

Fig. 2. Result of magnetostriction measurement of $LaCoO_3$ shown as a function of time, along with the magnetic field profiles generated using the EMFC method. The initial sample temperatures T_{ini} are varied from 5 K to 185 K

tion of plateaux of magnetostrictions. Considering that the magnetization below 200 T is far from the full polarization of the spin-states, further orderings of excitons are expected to appear above 200 T.

The experimental investigation has been challenging due to the need for very high magnetic fields beyond 100 T which is necessitated by the large spin-gap of ~100 K. Besides, one needs to probe the exciton states at such high magnetic fields. As solutions to these difficulties, recently, we reported the generation of 1200 T with electromagnetic flux compression (EMFC) method using a newly installed capacitor banks system in ISSP [3]. Furthermore, we succeeded in implementing a state-of-the-art high-speed 100 MHz strain gauge using fiber Bragg grating (FBG) and optical filter method, which have enabled us to measure magnetostriction in the μs-pulsed 1000 T environment [4]. Magnetostriction is a crucial probe of the exciton states because the density of excitons is coupled to the lattice volume of $LaCoO_3$, where exciton and bi-exciton states have larger ionic volumes with the occupation of eg orbitals that is spatially more extended than t2g orbitals as can be seen in the correspondence of spin-states and exciton states. Solidifications and Bose-Einstein condensations of excitons result in plateaus and slope of exciton density. Thus, we expect that they also result in plateaus and slope in magnetostriction curves at very low temperatures. Note that the correspondences are analogs to the magnetization plateaus and slopes in magnon solids and superfluids, respectively.

The results of magnetostriction measurements up to 600 T are presented in Fig 2. The new features indicating magnetic field induced phase transitions are observed. We summarize the obtained results in the present and previous studies on a magnetic field – temperature plane as shown in Fig. 3.

In addition to the data up to 600 T for the α phase and the β phase, we found novel phase termed γ phase. The variety of phases indicates the exotic ordering of the exciton degree of freedom in $LaCoO_3$. We qualitatively discuss the possibility of two kinds of spin-triplet exciton condensation realized in $LaCoO_3$ corresponding to the β phase and the γ phase. We attributed the origin of the α phase to be a crystallization of excitons. The study indicates the complicated interactions and symmetry breakings are in play in $LaCoO_3$ placed at ultrahigh magnetic fields [5].

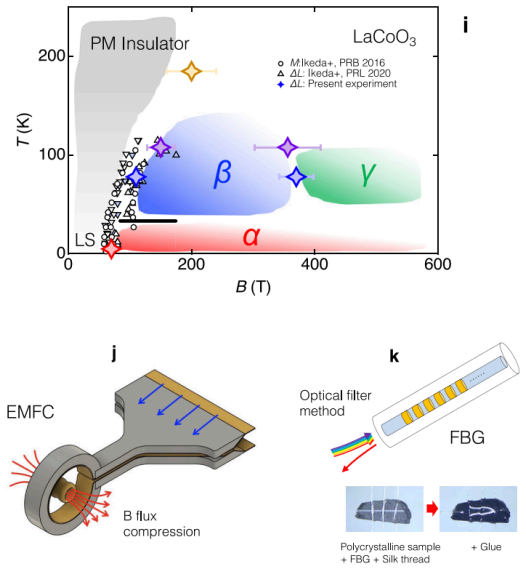

Fig. 3. Summary of the magnetostriction measurement of $LaCoO_3$ on a magnetic field-temperature plane up to 600 T along with the previously obtained data using magnetization and magnetostriction measurements

References

[1] A. Ikeda, T. Nomura, Y. H. Matsuda, A. Matsuo, K. Kindo, and K. Sato, Phys. Rev. B **93**, 220401(R) (2016).
[2] A. Ikeda, Y. H. Matsuda, and K. Sato, Phys. Rev. Lett. **125**, 177202 (2020).
[3] D. Nakamura, A. Ikeda, H. Sawabe, Y. H. Matsuda, and S. Takeyama, Rev. Sci. Instrum. **89**, 095106 (2018)
[4] A. Ikeda, T. Nomura, Y. H. Matsuda, S. Tani, Y. Kobayashi, H. Watanabe, and K. Sato, Rev. Sci. Instrum. **88**, 083906 (2017).
[5] A. Ikeda, Y. H. Matsuda, K. Sato, Y. Ishii, H. Sawabe, D. Nakamura, S. Takeyama, and J. Nasu, Nat. Commun. **14**, 1744 (2023).

Authors
A. Ikeda[a], J. Nasu[b], and Y. H. Matsuda
[a]University of Electro-Communications
[b]Tohoku University

Closing the Hybridization Charge Gap in the Kondo Semiconductor SmB_6 with an Ultrahigh Magnetic Field

Y. Matsuda Group

In materials with strong electron correlation, the nontrivial energy-band structure beyond the single-electron picture gives rise to exotic properties. SmB_6 is a typical Kondo semiconductor, whose hybridization gap has been estimated to be 5–20 meV. In addition to the strong electron correlation in SmB_6, the valence fluctuation of the Sm ion and possible topological surface state induce a complicated energy band structure. Under sufficiently high magnetic fields, the energy bands are shifted by the Zeeman effect and the evolution in magnetoresistance gives information to understand the complicated electronic states. However, an ultra-high magnetic fields above 100 T is required to achieve the field-induced semiconductor–metal (S–M) transition, which leads to the difficulty in observing the details of the evolution of the magnetoresistance up to the S–M transition in SmB_6 with high sensitivity.

In this research, we utilized the electromagnetic flux-compression (EMFC) technique [1] to generate ultra-high magnetic fields up to 320 T. The high-frequency electrical resistivity was measured using a contactless radio-frequency impedance measurement method developed by the authors [2], which demonstrates the observation of the upper critical magnetic field in cuprate superconductor [3] and the S–M phase transition in narrow-gap semiconductor [4]. The measurement SmB_6 sample (typically $1 \times 1 \times 0.05$ mm^3) was mounted on a self-resonant spiral probe coil with the diameter of 1 mm so that the ⟨100⟩ axis was parallel to the magnetic field. A radio-frequency voltage tuned around 700 MHz was applied to the probe coil and the reflected signal was acquired by the digital oscilloscope. The amplitude of reflected signal was obtained by the numerical lock-in method, and then converted to electrical resistivity by using the temperature dependence of signals measured just before applying the pulsed magnetic field.

Figure 1 shows the magnetic field dependence of the high-frequency electrical resistivity at 6.5 K, 16 K and 24 K (initial temperature just before applying the pulsed magnetic field) obtained from independent EMFC experiments up to 320 T [5]. The AC (50 kHz) magnetoresistances up to 55 T generated by the non-destructive pulsed magnet are also presented for comparison (black curves). At 16 K and 24 K, the data obtained by the EMFC and non-destructive magnet

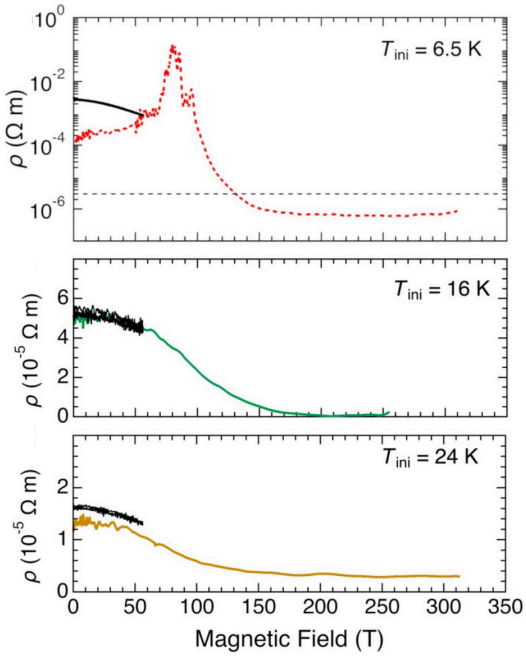

Fig. 1. Magnetic field dependence of the electrical resistivity at 6.5 K, 16 K, and 24 K. The AC magnetoresistances with 50 kHz up to 55 T generated by the non-destructive pulsed magnet are also presented for comparison (black curves).

experiments coincide well each other, indicating the high reliability of the results of EMFC experiments. The high-frequency resistivity gradually decreases with increasing the magnetic field and the field-induced S–M transition appears around 180 T by closing the hybridization gap in SmB_6. On the other hand, at 6.5 K, the resistivity obtained by the EMFC experiments significantly increases up to ~80 T, different from the result of non-destructive magnet experiment. This indicates a significant frequency dependence of electrical resistivity at low temperatures, and the scattering process for the carriers changes around 80 T at low temperatures. This is also suggested by an anomaly of temperature dependence of the electrical resistivity around 12.5 K under zero magnetic field.

Figure 2 presents the phase diagram of SmB_6 constructed based on the experimental findings in the present research

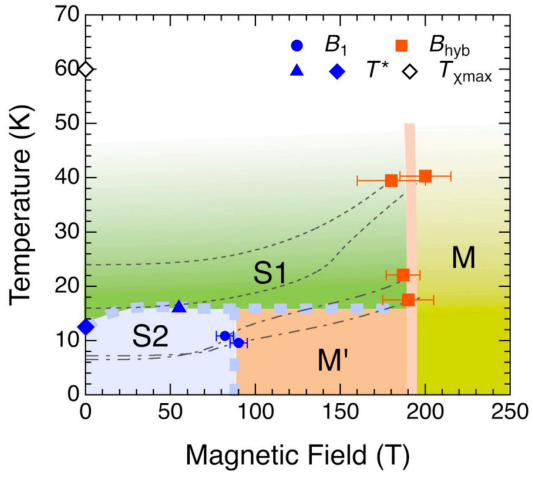

Fig. 2. Temperature–magnetic field phase diagram of SmB_6. B_1 (closed circle) and B_{hyb} (closed square) are taken from the results of the EMFC experiments. critical temperature T^* (closed triangle and diamond) is taken from the nondestructive magnet and PPMS experiments. The thin dashed-dotted and dotted curves indicate the temperature evolution during the magnetic-field pulse. Each state is separated by bold guidelines for a clear view, whose identifications are described in the main text.

[5]. Four black dashed-dotted and dotted curves represent the temperature evolution in the sample during the independent EMFC experiments, which arises from the extremely short pulse of the magnetic field generated by the EMFC technique.

By connecting the boundary points (the fields exhibiting the anomalies in the resistivity), four independent states (S1, S2, M′, and M) are defined in the phase diagram. Semiconducting state S1 is phenomenologically characterized by frequency-independent magnetoresistance and metallization at B_{hyb} ~ 180 T. The high-field M phase is likely to be a normal paramagnetic metal. The low-temperature semiconducting state S2 exhibits frequency-dependent magnetoresistance, and becomes metallic in the low-frequency transport at B_1 although the hybridization gap is still open. We suggest that the observed transition at B_1 relates with the energy scale of quasiparticles such as the spin polaron in the in-gap state.

References

[1] D. Nakamura *et al.*, Rev. Sci. Instrum. **89**, 95106 (2018).
[2] D. Nakamura, M. M. Altarawneh, and S. Takeyama, Meas. Sci. Technol. **29**, 035901 (2018).
[3] D. Nakamura *et al.*, Sci. Rep. **9**, 16949 (2019).
[4] D. Nakamura *et al.*, Phys. Rev. Lett. **127**, 156601 (2021).
[5] D. Nakamura *et al.*, Phys. Rev. B **105**, L241105 (2022).

Authors
D. Nakamura[a], A. Miyake, A Ikeda[b], M. Tokunaga, F. Iga[c], and Y. H. Matsuda
[a]RIKEN Center for Emergent Matter Science
[b]University of Electro-Communications
[c]Ibaraki University

Gradual Charge Order Melting in $Bi_{0.5}Ca_{0.5}MnO_3$ Induced by Ultrahigh Magnetic Fields

Y. H. Matsuda Group

Perovskite-type manganite series $AMnO_3$ (A = non magnetic ion) is the long standing one of the central subjects in condensed matter physics. Because of the coupling among the spin, charge, and orbital degrees of freedom, a lot of abundant exotic physical phenomena appear.

Electronic ground state of perovskite-type manganites is determined by the balance of the several interactions such as the Jahn-Teller coupling, on-site and inter-site Coulomb repulsion, superexchange interaction, and double exchange interaction.

Magnetic field effect on the ground state is significantly important subject in the perovskite-type manganites. The melting of the charge ordered (CO) state by applying magnetic fields is one of the central issues. This CO melting phenomenon sometimes accompanies the giant resistance change which is known as the colossal magnetoresistance.

The CO state in the perovskite-type manganites including Bi ions as A site ($Bi_{1-x}AE_xMnO_3$; AE = Ca or Sr) is more stable than that in the manganites including rare earth ions as A site ($Ln_{1-x}AE_xMnO_3$; Ln = rare earth element). The transition temperature of CO in $Bi_{0.5}Ca_{0.5}MnO_3$ (T_{CO} = 322 K) is higher than that in most of the rare earth systems with x = 0.5. The detailed investigation of the magnetic field effect on the CO phase in perovskite-type manganites with Bi ions would be interesting. However, the ultrahigh magnetic fields exceeding 100 T are needed for that investigation [1,2].

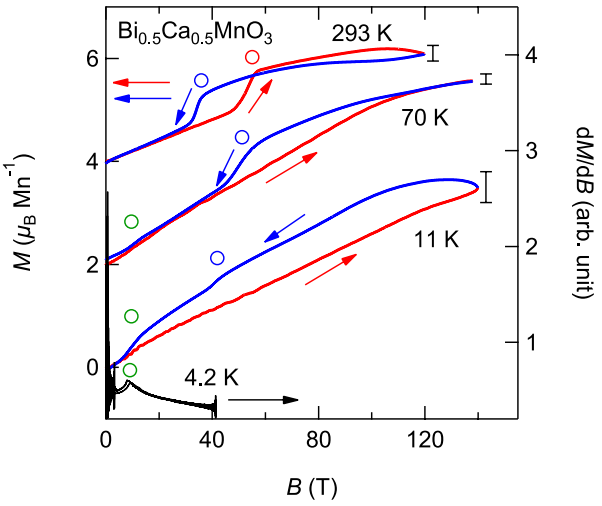

Fig. 1. Magnetization curves at 293 K (up to 120 T), 70 K (140 T), and 11 K (140 T). Red and blue lines represent the field ascending and descending processes, respectively. Black line is the dM/dB at 4.2 K up to 40 T measured by the nondestructive method. Critical fields are marked by red and blue open circles in the field ascending (B_c^{up}) and descending processes (B_c^{down}), respectively. Green open circles mark the critical field of the metamagnetic transition which appears around 10 T below T_N. The estimated error bar is shown for each measurement.

In this research [3], we tried to reveal the magnetic properties of $Bi_{0.5}Ca_{0.5}MnO_3$ under ultrahigh magnetic fields by means of the magnetization measurements up to 140 T over a wide temperature range from 11 to 293 K. We prepared the single crystals by Bi_2O_3 flux method, and the sample characterization was performed by XRD, SEM, and magnetic susceptibility measurement by MPMS. The powder sample prepared by crushing and grinding the obtained crystals was used for the magnetization measurements.

We revealed that the CO in $Bi_{0.5}Ca_{0.5}MnO_3$ can be melted by applying the magnetic field at the room temperature (293 K) (Fig. 1). It is observed as the metamagnetic transition. At low temperatures, the CO melting phase transition in the field ascending process becomes broad. However, the CO reformation can be observed clearly in the field descending process (Fig. 1). This asymmetric broadening phenomenon can be understood by the gradual CO melting induced by the ultrahigh magnetic fields.

This asymmetric broadening of the CO melting is possibly explained by the spatial inhomogeneity of charge distribution. In perovskite-type manganites, a spatial inhomogeneity of charge distribution the one of the attractive subjects and the important factor for the electronic ground state and phase transitions. The spatial inhomogeneity will be

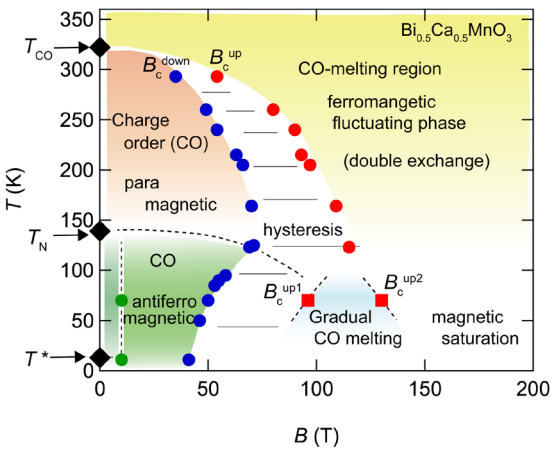

Fig. 2. B-T phase diagram constructed. Electronic and magnetic states in the low-field region have been reported in several previous studies.

frozen by decreasing temperature, therefore the phase transition can be broad in the field ascending process. On the other hand, the spatial inhomogeneity will become less because the electron becomes itinerant in the CO melting region under the ultrahigh magnetic field. As a result, the metamagnetic transition can be sharp in the field descending process.

Another possible reason related to the slow dynamics is the critical slowing down owing to the quantum criticality of antiferromagnetic order.

Finally, we constructed the B-T phase diagram of $Bi_{0.5}Ca_{0.5}MnO_3$ (Fig. 2).

For further investigation of the unusual CO melting phenomenon, the magnetostriction, resistivity, and XRD measurement under ultrahigh magnetic fields will be performed.

References

[1] A. Kirste *et al*., Phys. Rev. B **67**, 134413 (2003).
[2] S. Takeyama *et al*., J. Phys. Soc. Jpn. **81**, 014702 (2011).
[3] Y. Ishii, A. Ikeda, M. Tokunaga, K. Kindo, A. Matsuo, and Y. H. Matsuda, J. Phys. Soc. Jpn. 92, 074702 (2023).

Authors

Y. Ishii, A. Ikeda[a], M. Tokunaga, K. Kindo, A. Matsuo, and Y. H. Matsuda
[a]University of Electro-Communications

Metastable Quantum Phase in Adiabatic Condition with the Spin-Lattice Separation

Y. H. Matsuda, Kohama, and Kindo Group

Several low-dimensional spin systems exhibit exotic magnetization processes such as magnetization plateaux as a result of the appearance of exotic quantum phases. The spin-ladder materials are intriguing because they possess intermediate properties between one- and two-dimensions. The two-leg spin-ladder compound 3, 3′, 5, 5′-tetrakis(N-tert-butylaminoxyl)biphenyl: $C_{28}H_{42}N_4O_4$ (BIP-TENO) was synthesized as the first S = 1 two-leg spin ladder, where S is the spin quantum number. In BIP-TENO, the nontrivial 1/4 magnetization plateau was observed in the magnetic field range from 42 to 66 T and theoretically analyzed [1]. To explain the 1/4 plateau, the authors of Ref. [1] introduced the second-nearest-neighbor (diagonal direction) and third-nearest-neighbor (leg direction) exchange interactions and found that the third-nearest-neighbor exchange interaction is more essential for the appearance of the 1/4 plateau. They obtained the magnetization by a numerical diagonalization. Although further successive phase transitions to the 1/2 and 3/4 plateau states are theoretically predicted [1], they were never experimentally observed because the required magnetic field is as strong as 150 T, which is only available employing a destructive manner [2]. In the present study, the entire magnetization process of BIP-TENO is investigated in ultrahigh magnetic fields of up to 150 T using the single-turn coil that is one of the destructive means for ultrahigh magnetic field generation. It is unveiled that 1/3 and 2/3 plateaus appear in addition to the previously discussed 1/4, 1/2, and 3/4 plateaus. Moreover, the 1/3 and 2/3 plateaus are found to appear only when the magnetic field is swept in a microsecond timescale. The adiabatic condition is likely to be necessary for its observation, suggesting that the newly observed plateaus are metastable states.

The single crystals of BIP-TENO were used. The typical dimensions of the crystal used are 2 ~ 4 × 0.5 × 0.2 mm^3 and the direction of the long side is parallel to the c-axis. Three or four single crystals were used for the magnetization measurement to obtain the larger signal. In the pulsed-field experiments, magnetic fields (B) were applied parallel to the c-axis of the crystal that is parallel to the leg direction of the spin ladder. The ultrahigh magnetic fields were generated using the single-turn coil. The magnetization was measured using a self-compensated parallel-type pickup coil. The sample temperature was lowered by directly immersing the sample in liquid helium or by putting the sample in flowing cold helium gas.

Figure 1 shows the magnetization process measured at 4.2 K with the single-turn coil up to approximately 100 T (a red curve) [3]. The pulse duration is about 7 μs. In the figure, the previously reported magnetization curve at 1.3 K [1] is also shown for comparison (a green curve). A nondestructive magnet with a 5 ms duration was used in this measurement.

The 1/4 plateau is observed in both (red and green) curves. The striking difference is seen in the length of the plateau: the plateau ends at around 50 T and a new plateau appears after that in the red curve, while it continues to around 70 T. One may wonder whether this distinct difference can be caused by the temperature difference because the fast magnetic field changes potentially induce the temperature change due to the magnetocaloric effect. Hence, we investigated the magneto-caloric effect and found that although temperature decreases by several degrees with increasing the magnetic field in adiabatic conditions, the plateau lasts at least up to 60 T and no new plateau emerges at around 50 T [3]. This fact excludes the possibility that the different temperatures cause the different magnetization processes.

The measurement of the magnetostriction solved this mysterious question. We found that the leg direction of the crystal shrinks when the spin gap closes. The fiber Bragg grating method was utilized. The shrinkage of the lattice also causes a dissipation process and causes some heat production, which was detected in our magnetocaloric effect.

Figure 2 shows the shrinkage of the lattice when a pulsed magnetic field is applied as a function of time [3]. The lattice shrinks when a magnetic field is applied slowly

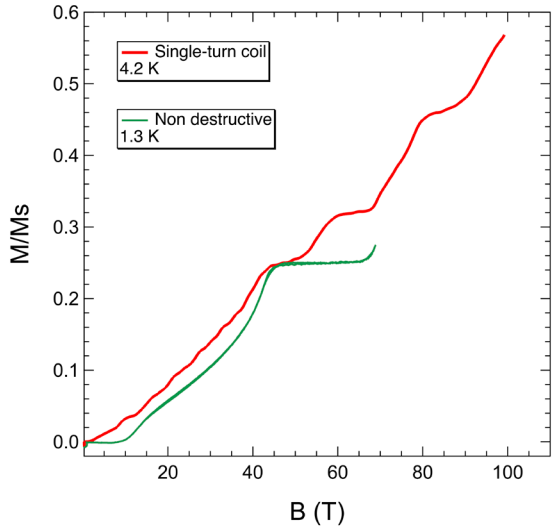

Fig. 1. Magnetization process of a single crystal of BIP-TENO measured within 7 μs using the single-turn coil (red curve). The green curve shows the magnetization process of BIP-TENO measured in a non- destructive pulsed magnetic field with a duration of 5 ms.

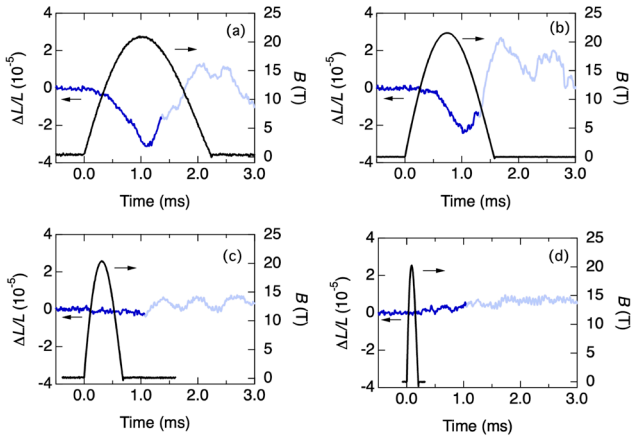

Fig. 2. The magnetostriction ΔL / L and the magnetic field are plotted as a function of time. The striction is seen in high magnetic fields as shown in (a) and (b), while it is absent when the magnetic field pulse is short as shown in (c) and (d).

(Fig. 2 (a)). However, the response of the lattice is delayed for the shorter field pulse (Fig. 2 (b)), and then, interestingly, the lattice doesn't move if the magnetic field pulse is short enough (Fig. 2 (c.) (d)). The threshold time is around 1 ms, which gives the answer to why the two different magnetization processes are observed with fast and slow magnetic field pulses.

The red curve in Fig. 1 is a magnetization process for the spins at the original lattice sites. The length of the 1/4 plateau suggests the strength of the interaction given by the zero-field crystal lattice. The new plateau following the 1/4 plateau seems to be assigned to the 1/3 plateau which has been proposed to emerge in a recent theoretical study [4]. The longer 1/4 plateau seen in the green curve in Fig. 1 is explained by an enhancement in the exchange interaction along the leg direction due to the contraction of the leg direction by a magnetic field.

In summary, the slow contraction of the crystal in the leg direction by the application of a magnetic field stabilizes the 1/4 plateau and hinders the following 1/3 plateau. The novel 1/3 plateau is a metastable state where the crystal lattice maintains the original form within a short time in the range of microseconds. This metastable quantum phase is a result of the spin-lattice separation and has hardly ever been observed before.

References

[1] T. Sakai, N. Okazaki, K. Okamoto, K. Kindo, Y. Narumi, Y. Hosokoshi, K. Kato, K. Inoue, and T. Goto, Phys. B: Condens. Matter **329**, 1203 (2003).
[2] N. Miura, T. Osada, and S. Takeyama, J. Low Temp. Phys. **133**, 139 (2003).
[3] K. Nomura, Y. H. Matsuda, A. Ikeda, Y. Kohama, H. Tsuda, N. Amaya, T. Ono, and Y. Hosokoshi, Phys. Rev. B **105**, 214430 (2022).
[4] H. Kohshiro, R. Kaneko, S. Morita, H. Katsura, and N. Kawashima, Phys. Rev. B **104**, 214409 (2021).

Authors
K. Nomura, Y. H. Matsuda, A. Ikeda[a], Y. Kohama, H. Tsuda[b], T. Ono[c], and Y. Hosokoshi[c]
[a]The University of Electro-Communications
[b]National Institute of Advanced Industrial Science and Technology
[c]Osaka Metropolitan University

Field-Induced Insulating State in a Topological Insulator BiSb Alloy

Tokunaga Group

Applying high-enough magnetic fields on metals realizes the quantum limit states, in which all the carriers are accommodated in the lowest Landau level. Since the carriers are confined in the smallest cyclotron orbit, the kinetic degree of freedom normal to the field is suppressed in this state. Thus, the ratio between Coulomb interaction and bandwidth, a measure of electron correlation, grows as the field increases. Such strong correlation in the quantum limit state can realize anomalous quantum state, like the fractional quantum Hall effect in two-dimensional electron systems. On the other hand, it is an open question what kind of quantum states can be realized by the effect of a strong correlation in the quantum limit state of a three-dimensional system [1]. In particular, quantum limit states of semimetals in which electrons and holes coexist are ideal platforms for realizing novel quantum states.

In this context, we focused on narrow gap semiconductors in which the gap can be closed by external magnetic fields, as illustrated in Fig. 1. Continuous valence and conduction bands at a zero magnetic field split into discrete Landau sub-bands in finite magnetic fields. These Landau sub-bands can be continuously shifted by a magnetic field with the Zeeman and cyclotron energies. We can close the gap in some materials at a specific field, causing semiconductor-semimetal transition at a critical field of B_c. The realized semimetallic state is a spin-polarized quantum limit state. We can expect the emergence of a novel quantum state above B_c.

As a target, we focus on a BiSb alloy. The BiSb alloys have attracted renewed interest after recognized as the first example of topological insulators [2]. Applying a magnetic field to this system can close the gap due to the level crossing of spin-split Landau levels in the conduction and valence bands. We found that further magnetic field application realizes an insulating state in this realized field-induced semimetallic state.

Figure 2 shows longitudinal magnetoresistance in a single crystal of $Bi_{1-x}Sb_x$ (x = 0.10) at various temperatures

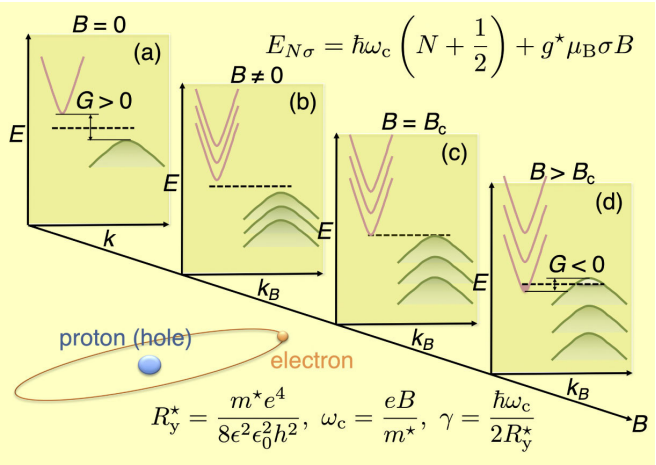

Fig. 1. Schematic of field-induced semiconductor-semimetal transition. Application of magnetic field changes continuous dispersion at a zero magnetic field (a) to discrete Landau sub-bands (b). In some materials, we can close the gap at a critical field of B_c (c) and realize a spin-polarized quantum limit state in a semimetallic phase (d). As illustrated in the inset, the electron-hole system in semimetals can reproduce an electron-proton system in an extremely high magnetic field.

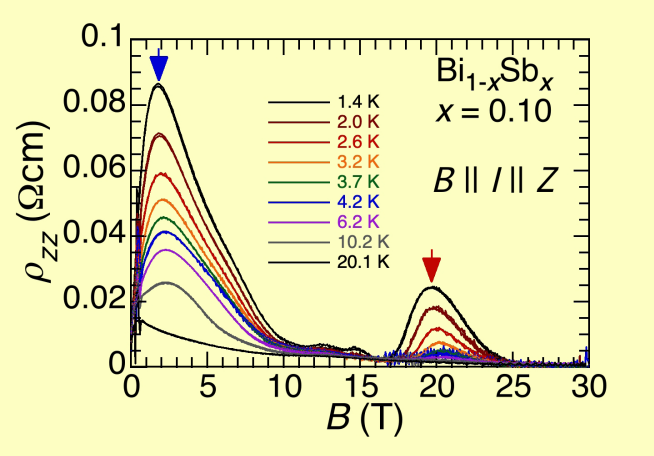

Fig. 2. Longitudinal magnetoresistance of $Bi_{1-x}Sb_x$ (x = 0.10) in a field along the three-fold rotational axis of the crystal. A semiconductor-semimetal transition is induced at 11 T. Additional insulating behavior appears at a field ~ 20 T below a temperature of 4 K, as marked with a red arrow.

[3]. Here, magnetic fields and electric currents are applied along the three-fold rotational axis of the crystal. In this field direction, Zeeman energy in the valence band is significantly larger than the cyclotron energy, so the application of the field higher than 11 T causes a semiconductor-semimetal transition at this field. Our results of magnetoresistance show metallic behavior above 11 T while causing insulating again at around 20 T and temperatures below 4 K.

This field-induced semimetallic state is a spin-polarized quantum limit state, in which we expect a strong correlation effect. The correlation effect in such an electron-hole system has been expected to host the BEC or BCS state of excitons (excitonic phase) at the vicinity of the zero-gap state. Estimation from our experimental results revealed that the binding energy between an electron and a hole becomes 0.3 meV, which is comparable to the thermal energy of 4 K. In addition, interparticle distance becomes also comparable with the thermal de Broglie length below 3 K. These estimations suggest possible emergence of the excitonic phase in BiSb.

The electron-hole systems of semimetals in magnetic fields can reproduce the electron-proton system under extremely high magnetic fields [4]. Suppose the effect of a magnetic field is measured by the ratio of cyclotron energy to Rydberg energy. In that case, the magnetic field effect is amplified in semimetals with small effective mass and large relative permittivity. Applying a magnetic field of 20 T to this BiSb alloy results in this ratio γ of ~ 4000, corresponding to a situation in which a magnetic field of one billion Tesla is applied to hydrogen atoms. What happens when the number of positive and negative carriers is continuously increased from zero under such conditions? Our results in a semimetal may reproduce the quantum state exhibited by hydrogen atoms in a billion Tesla magnetic field.

References

[1] B. I. Halperin, Jpn. J. Appl. Phys. **26**, 1913 (1987).
[2] D. Hsieh *et al.*, nature **452**, 970 (2008).
[3] Y. Kinoshita *et al.*, Phys. Rev. B **107**, 125140 (2023).
[4] Y. Kuramoto, *Hankinzokuchu no Densi-Seikou Soukan to Chouonpa no Kyodai Ryousigensui* (in Japanese) (Kyoritsu 1982).

Authors
Y. Kinoshita, T. Fujita, R. Kurihara, A. Miyake, Y. Izaki[a], Y. Fuseya[b], and M. Tokunaga
[a]Tokyo Institute of Technology
[b]University of Electro-Communications

Correlation-Driven Organic 3D Topological Insulator with Relativistic Fermions

Kohama and Kindo Group

Topological insulators (TIs) are a new class of materials that possess both bulk insulating and exotic surface/edge states. Conventionally, realizing a TI state usually requires a strong spin–orbit coupling (SOC) of heavy elements, leading to a band inversion and an insulating bulk gap. Consequently, it is challenging to observe a TI state and its unique physical features in light-atom materials, such as carbon-based systems, because of their weaker SOC. Recent theoretical studies propose a new pathway to realize a TI state via strong electron correlation, where the Coulomb interaction induces the bulk gap [1, 2]. Such correlation-driven TIs hold great scientific significance as they expand the scope of materials capable of forming TI states and potentially introduce new functions unique to correlated systems. An organic conductor α-$(BETS)_2I_3$ is a theoretical candidate for such correlation-driven TIs [3]. Nonetheless, experimental evidence to determine the accurate electronic state of this compound has been scant.

In our recent work [4], we performed magnetotransport measurement for α-$(BETS)_2I_3$ using pulsed high fields up to 60 T to clarify the low-temperature electronic state of this compound. Fig. 1a shows the longitudinal magnetoresistance (MR) measured at several temperatures. As shown in Fig. 1a, a large negative MR is observed below 4 K. This negative longitudinal MR resembles the MR induced by the "chiral anomaly" which is typically observed in three-dimensional (3D) Dirac or Weyl semimetals under parallel electric and magnetic fields (Fig. 1b). This result implies the presence of 3D relativistic particles (Weyl particles) in α-$(BETS)_2I_3$. The chiral-anomaly-induced negative MR is expected to be proportional to the square of the magnetic field. As shown in Fig. 1c, the inverse value of MR (written as MG in this report) at low temperatures is well-fitted by a quadratic function across a broad range of magnetic fields.

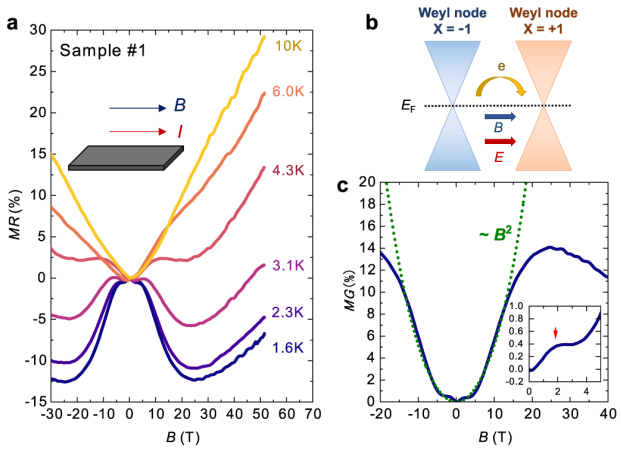

Fig. 1. **a** Longitudinal MR of α-$(BETS)_2I_3$ (I // B). The magnetic-field dependence of MR was measured at several temperatures. The quadratic negative magnetoresistance can be observed below 4 K. **b** Schematic of the charge flow induced by chiral magnetic effect (CME). In a magnetic field, the positive magnetoconductance (MG) due to the chiral anomaly flows between two Weyl nodes with different chirality $x = \pm 1$. **c** MG at 1.6 K. The green dashed line denotes the fitting curve $MG = C_aB^2$ with $C_a = 4.92 \times 10^{-4}$. Below 15 T, MG follows B^2 dependence, indicating the CME-induced MR. Inset: Expanded figure of MG at 1.6 K. The hump-like positive MG can be observed below 5 T, implying weak localization.

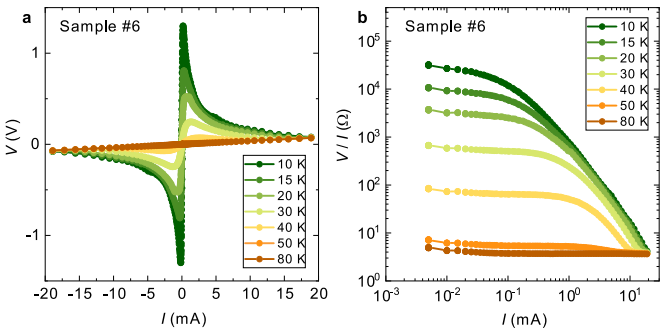

Fig. 2. **a** Current–voltage (I – V) characteristic measured at several temperatures using the four-terminal dc method with constant currents. A nonlinear conduction effect is observed in the wide current range. **b** Current dependence of the sample resistance (V/I). In the low current region, V/I is a constant value followed by Ohm's law. As the applied current increases, the sample resistance decreases by several orders of magnitude.

Moreover, unlike the longitudinal MR, the transverse MR of this compound exhibits positive [4], which is also consistent with the characteristics of the 3D-Dirac/Weyl system. Our findings suggest that the band structure of α-$(BETS)_2I_3$ has a Dirac-type dispersion with a very small gap, coinciding with the correlation-induced TI state theorized for this compound.

Next, we measured the current-voltage (I-V) character of this compound to observe a unique functionality of the correlation-driven TI state. As shown in Fig. 2a and 2b, we found that this compound shows a significant negative-differential resistance at low temperatures where a resistance (V/I) reduces by 3~4 orders of magnitude upon current application. This indicates that the low-temperature insulating state of this compound can be switched to a metallic state under external currents. Such metal-insulator switching due to current application is a phenomenon often seen in materials becoming insulating due to electron correlation [5] and is not a characteristic of conventional TIs.

Our experimental results provide evidence for the theoretical prediction that α-$(BETS)_2I_3$ is a TI. This is the first discovery of a TI composed of organic materials. Furthermore, this TI state can be manipulated into other electronic states using external fields, which has a potential for industrial application. We desire to deepen our understanding of the physical properties of organic TIs and advance further material development through research on analog compounds.

References

[1] S. Raghu, X. L. Qi, C. Honerkamp *et al.*, Phys. Rev. Lett. **100**, 156401 (2008).
[2] D. Ohki, K. Yoshimi, and A. Kobayashi, Phys. Rev. B. **105**, 205123 (2022).
[3] S. Kitou, T. Tsumuraya, H. Sawahata *et al.*, Phys. Rev. B **103,** 035135 (2021).
[4] T. Nomoto, S. Imajo, H. Akutsu *et al.*, Nat. Commun. **14**, 2130 (2023).
[5] F. Sawano, I. Terasaki, H. Mori *et al.*, Nature **437**, 522 (2005).

Authors

T. Nomoto, S. Imajo, H. Akutsu[a], Y. Nakazawa[a], and Y. Kohama
[a]Osaka University

Rise of Nonlinear Soft X-Ray Spectroscopy

I. Matsuda Group

X-ray spectroscopy has been a powerful technique to probe electronic states in materials. The light-matter interaction is based on a linear-response but it becomes non-linear when the intensity of incident light is significantly high. Recently, developments of X-ray free electron laser (XFEL) have led to our observation of the second harmonic generation, one of the well known non-linear optical phenomena, with soft X-ray (SX-SHG)[1]. A SX-SHG event occurs only when the inversion symmetry of the targeted system is broken and the signal is element-specific. These unique characters have pushed to apply SX-SHG for spectroscopy of materials science. However, it is often difficult to acquire a pure SX-SHG beam from a sample when the intensity is as small as second-harmonic radiation, generated on off-axis at the undulators. Such signal contamination is harmful for discussing genuine properties of SHG from any target sample. To overcome the situation, we developed and installed a new ellipsometry method for soft X-ray SHG experiment, as shown in Fig.1, to suppress the contribution of second-harmonic light from the XFEL beamline [2]. By the collaboration with RIKEN, we have also developed an experimental chamber of SX-SHG and opened for the SACLA users. We have successfully detected the broken inversion symmetry in the polar metal phase of $LiOsO_3$ with an enhanced feature above the Li K-edge that reflects the degree of Li atom displacement [3]. In a noncentrosymmetric crystal of $LiNbO_3$, elemental contributions by lithium and niobium were apparently distinguished by energy dependent SX-SHG measurements [4]. We have also probed the lithium mobility at a solid electrolyte surface to develop the Li-ion battery [5].

These research have applied the novel measurement method for investigation of crystallographic or electronic properties. The sensitivity to magnetism has remained elusive. Though a magnetic moment as an axial vector does not break the bulk inversion symmetry, it lowers the symmetry at interfaces, and thus should make additional contributions to SHG. While X-ray linear spectroscopies such as X-ray magnetic circular dichroism are useful to element-selectively study the magnetic properties of a material, it averages inevitably information over a certain depth along the incident light. To meet the demand of

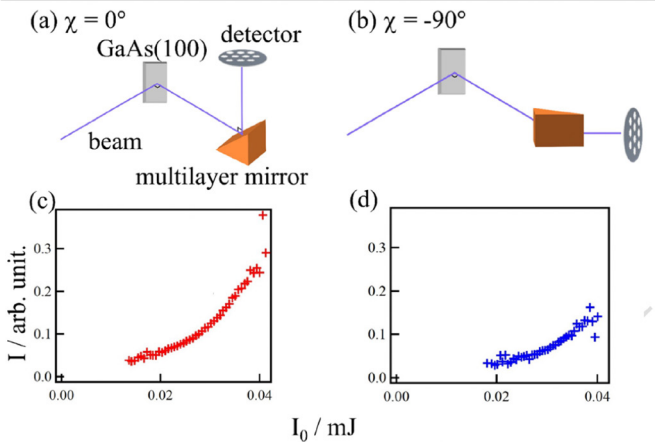

Fig. 1. Soft X-ray SHG data of GaAs(100) taken at the As M absorption edge, recorded with the ellipsometry method. The incident photon (I_0) beam was set at hν = 75 eV and the SHG signal (I) was detected at 2hν = 150 eV. The measurement geometries for the ellipsometry rotation angles at (a) χ = 0° and (b) −90°. Intensity curves of the SHG signals are shown in (c) and (d) that were taken by (a) and (b), respectively.

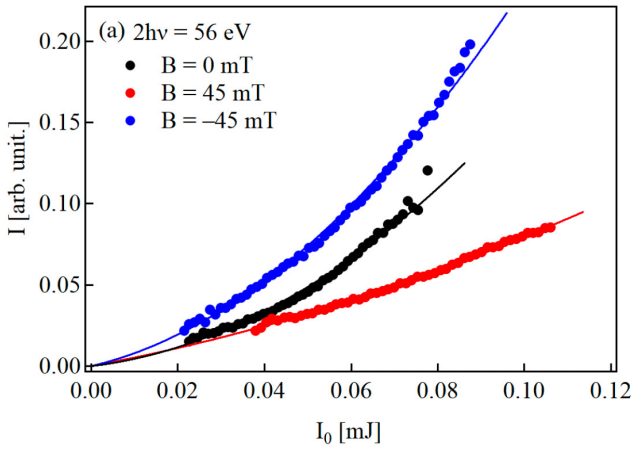

Fig. 2. SX- magnetization induced SHG (MSHG) from the [Au/Fe/MgO]$_4$ sample. 2hν intensity plot with respect to the incident beam intensity I_0 at 2hν = 56 eV under magnetic field as indicated. Photon energy of 56 eV corresponds to the Fe M-edge resonance. Solid curves represent the results of fitting with nonlinear curves.

frontier technology, such as spintronics, that utilizes magnetic materials with complicated multilayered structure, it is, thus, useful to develop an element-selective method that can exclusively probe interface magnetism. We developed a magnetization induced SHG for soft X-ray (SX-MSHG) measurement system and made a demonstration for an Fe-based multilayer samples with broken inversion symmetry [6]. At the Fe M-edge resonance condition, we observed, as shown in Fig. 2, a clear dependence of SX-MSHG on the direction of applied magnetic field, even though the field was along the hard magnetization axis and thus the magnetization was only a small fraction of the saturation value. The results indicate high sensitivity of the measurement likely due to inner-shell resonance. By further deepening the understanding of its unique characteristics, SX-MSHG could be developed into a solid technique to element-selectively probe interface magnetism.

Through the technical efforts, research of the nonlinear optical effect in the soft X-ray region has evolved into a method of nonlinear soft X-ray spectroscopy. The unique characters of both the interface- and element-selectivity are useful for unveiling electronic and magnetic properties of the complicated compounds that provide various functionalities. Nonlinear X-ray spectroscopy is expected to become one of the standard analysis methods for materials science.

References

[1] Sh. Yamamoto, T. Omi, H. Akai, Y. Kubota, Y. Takahashi, Y. Suzuki, Y. Hirata, K. Yamamoto, R. Yukawa, K. Horiba, H. Yumoto, T. Koyama, H. Ohashi, S. Owada, K. Tono, M. Yabashi, E. Shigemasa, S. Yamamoto, M. Kotsugi, H. Wadati, H. Kumigashira, T. Arima, S. Shin, and I. Matsuda, Phys. Rev. Lett. **120**, 223902 (2018).
[2] T. Sumi, M. Horio, T. Senoo, T. Wada, Y. Tsujikawa, X. Zhang, P. Manset, M. Araki, Y. Hirata, W. S. Drisdell, J. W. Freeland, A. Amado, M. Zuerch, Y. Kubota, S. Owada, K. Tono, M. Yabashi, C. P. Schwartz, and I. Matsuda, e-J. Surf. Sci. Nanotechnol. **20**, 25 (2022).
[3] E. Berger, S. Jamnuch, C. B. Uzundal, C. Woodahl, H. Padmanabhan, A. Amado, P. Manset, Y. Hirata, Y. Kubota, S. Owada, K. Tono, M. Yabashi, C. Wang, Y. Shi, V. Gopalan, C. P. Schwartz, W. S. Drisdell, I. Matsuda, J. W. Freeland, T. A. Pascal, and M. Zuerch, Nano Letters **21**, 6095 (2021).
[4] C. B. Uzundal, S. Jamnuch, E. Berger, C. Woodahl, P. Manset, Y. Hirata, T. Sumi, A. Amado, H. Akai, Y. Kubota, S. Owada, K. Tono, M. Yabashi, J. W. Freeland, C. P. Schwartz, W. S. Drisdell, I. Matsuda, T. A. Pascal, A. Zong, and M. Zuerch, Phys. Rev. Lett. **127**, 237402 (2021).
[5] C. Woodahl, S. Jamnuch, A. Amado, C. B. Uzundal, E. Berger, P. Manset, Y. Zhu, Y. Li, D. D. Fong, J. G. Connell, Y. Hirata, Y. Kubota, S. Owada, K. Tono, M. Yabashi, S. Tepavcevic, I. Matsuda, W. S. Drisdell, C. P. Schwartz, J. W. Freeland, T. A. Pascal, A. Zong, and M. Zuerch, Nat. Mater. (2023). https://doi.org/10.1038/s41563-023-01535-y

[6] T. Sumi, M. Horio, T. Senoo, Y. Kubota, G. Yamaguchi, T. Wada, M. Miyamoto, K. Yamaguchi, Y. Tsujikawa, Y. Sato, M. Niibe, Y. Hirata, Y. Miyauchi, D. Oshima, T. Kato, S. Owada, K. Tono, M. Yabashi, and I. Matsuda, Appl. Phys. Lett. **122**, 171601 (2023).

Author
I. Matsuda

Real-Time Observation of the Woodward-Hoffmann Rules for 1,3-Cyclohexadiene by Femtosecond Soft X-Ray Transient Absorption

Itatani Group

The stereochemistry of pericyclic reactions is explained by orbital symmetry conservation, referred to as the Woodward-Hoffmann (WH) rules. Although these rules have been verified by the structures of reactants and products, the temporal evolution of the orbital symmetry during the reaction has not been clarified. Herein, we used femtosecond soft X-ray transient absorption spectroscopy to elucidate the thermal pericyclic reaction of 1,3-cyclohexadiene (CHD) molecules, *i.e.*, its isomerization to 1,3,5-hexatriene. In the present experimental scheme, the ring-opening reaction is driven by the thermal vibrational energy injected by photoexcitation to the Rydberg states at 6.2 eV and subsequent femtosecond relaxation to the ground state of CHD molecules. The direction of the ring opening, which can be conrotatory or disrotatory, was the primary focus (see Fig. 1), and the WH rules predict the disrotatory pathway in the thermal process.

We focused on the *K*-edge absorption of the carbon atom from the 1s orbital to vacant molecular orbitals around 285 eV, because the *K*-edge absorption energy depends on the local environment of a carbon atom and could be sensitive to the transient molecular structure [1]. We expect to identify the transient molecular structures by the *K*-edge absorption. The BiB_3O_6-based optical parametric chirped pulse amplifier is used to produce carrier-envelope phase-stable intense infrared pulses (center wavelength 1.6 μm, pulse energy 1 mJ, pulse duration 10 fs at 1 kHz). This output is focused into Ne-filled gas cell to produce soft-X-ray continua covering the carbon *K*-edge, and the transmitted spectrum through the CHD-filled gas cell is measured by a grating spectrometer. The second harmonic (wavelength 400 nm) from the Ti:sapphire laser amplifier is used to pump the CHD molecules by two-photon absorption. Figure 2 shows the stationary carbon *K*-edge absorption spectrum of CHD (upper panel) and the time-resolved difference spectra (ΔA) at the designated delay time (lower panel).

The ultrafast relaxation from the Rydberg states to the ground state with a time constant of 26 ± 7 fs is identified

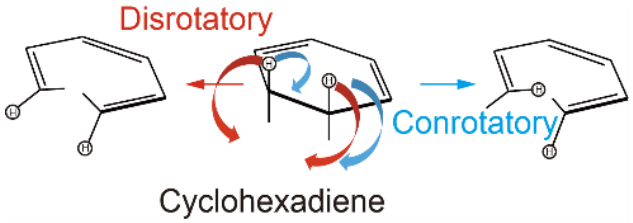

Fig. 1. Two ring-opening pathways of 1,3-cyclohexadiene (CHD) molecules

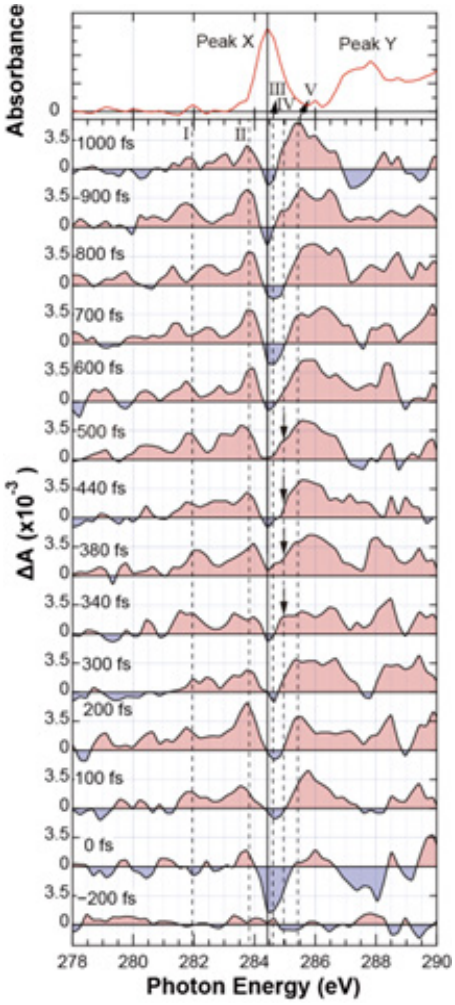

Fig. 2. Stational absorption spectrum and time-resolved ΔA spectra.

by the disappearance of the bleaching of peak X observed at 0 fs. Another interesting feature in the time-resolved ΔA spectra is that the induced absorption band temporally appears between 340 and 600 fs at a higher absorption energy than peak X indicated by the arrows in Fig. 2. A theoretical investigation predicts that the transient molecular structures along the disrotatory pathway have higher *K*-edge absorption than peak X, while those along the conrotatory pathway have lower. Therefore, we attributed the observed induced absorption to the structural change in the disrotatory pathway, which is consistent with the prediction by the W-H rules. The observed dynamics show that the CHD ring starts to open approximately 340 fs later upon photoexcitation. This agrees with the observations by time-resolved photoelectron and high-harmonic spectroscopies [2, 3].

References
[1] T. Sekikawa *et al.*, Phys. Chem. Chem. Phys. **25**, 8497 (2023).
[2] R. Iikubo *et al.*, Faraday Discuss. **194**, 147 (2016).
[3] K. Kaneshima *et al.*, Opt. Express **26**, 31030 (2018).

Authors
T. Sekikawa[a], N. Saito, Y. Kurimoto[a], N. Ishii[b], T. Mizuno, T. Kanai, J. Itatani, K. Saita[a], and T. Taketsugu[a]
[a]Hokkaido University
[b]National Institute for Quantum Science and Technolgy

Testing Electron-phonon Coupling for Superconductivity in Kagome Metal CsV_3Sb_5

Okazaki and Kondo Groups

In crystalline materials, electron-phonon coupling (EPC) is a ubiquitous many-body interaction that drives conventional Bardeen-Cooper-Schrieffer superconductivity. Recently, in a new kagome metal CsV_3Sb_5, superconductivity that possibly intertwines with time-reversal and spatial symmetry-breaking orders is observed [see phase diagram in Fig. 1a]. Density functional theory (DFT) calculation [1] predicted a weak EPC strength, λ, supporting an unconventional pairing mechanism in CsV_3Sb_5. However, experimental determination of λ is still missing, hindering a microscopic understanding of the intertwined ground state of CsV_3Sb_5. In this study, using 7-eV laser-based angle-resolved photoemission spectroscopy (ARPES) and Eliashberg function analysis, we experimentally extract the orbital- and momentum-dependent λ by determining the EPC-induced kinks in the electronic band structure.

We first present the Fermi surface (FS) topology of CsV_3Sb_5 in Fig. 1b. In agreement with DFT study and previous ARPES studies [1, 2], the Sb 5*p*-band forms a circular FS, marked as α, at the BZ center and the V 3d-bands yield hexagonal and triangular FSs, marked as β and δ in Fig. 1b, respectively. Figure 1c shows a typical ARPES intensity plot of the α band corresponding to the black cut shown in Fig. 1b. By fitting momentum distribution curves (MDCs) with a Lorentzian function as the yellow and black curves shown in Fig. 1c, the band dispersion $\omega(\boldsymbol{k})$ is extracted as the red curve in Fig. 1c and the single-particle self-energy, $\Sigma(\omega = E - E_F)$, is quantitively extracted in Fig. 1d. At $E_B \sim 32$ meV, a peak in the real part ReΣ(ω) and a step jump in the imaginary part ImΣ(ω) prove a strong coupling between electrons and bosonic modes [3], which are manifested as a kink in the band structure. As the kink is persistent above the CDW transition temperature and any magnetic orders are absent, we attribute it to EPC.

Next, we study the orbital-dependence of EPC by comparing the kinks on the α and β bands. As in Fig. 1e, ReΣ(ω) of the β band which is derived from V 3*d* orbitals shows a peak near $E_B \sim 12$ meV, suggesting a strong

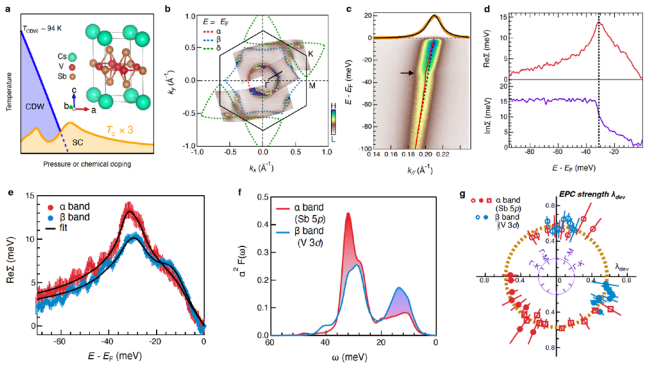

Fig. 1. Orbital and momentum dependence of EPC in CsV_3Sb_5 kagome superconductor. (a) Phase diagram and crystal structure (inset). (b) Fermi surface mapping with ARPES intensity integrated within $E_F \pm 5$ meV. (c) ARPES intensity plot for a black cut in (b). (d) Extracted self-energy from the ARPES intensity plot shown in (c). (e) Real-part self-energy for the α and β bands along the Γ-K direction. (f) Extracted Eliashberg function for the α and β bands by fitting ReΣ(ω) in (e). (g) EPC strength λ_{dev} at different momenta on the α and β Fermi surfaces.

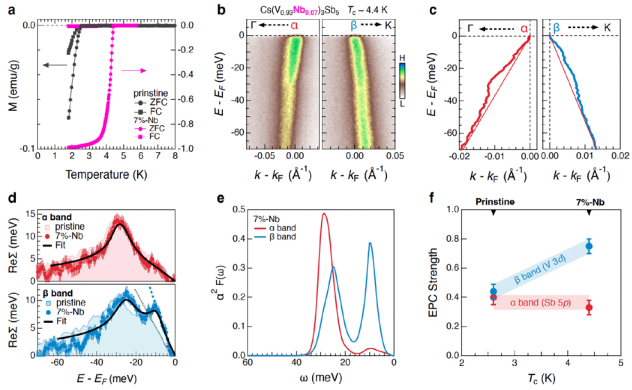

Fig. 2. Orbital and energy selective enhancement of EPC in 7%-Nb doped CsV_3Sb_5. (a) Temperature dependence of magnetic susceptibility. Both zero-field cooling (ZFC) and field cooling (FC) curves are presented. (b) ARPES intensity plots of the α and β bands along the Γ-K direction. (c) Extracted band dispersions. (d) Extracted real-part self-energy for the α (top panel) and β (bottom panel) bands. Colored shadows are the corresponding ReΣ(ω) for pristine CsV_3Sb_5. The dashed lines in bottom panel represent the slope of ReΣ(ω) at E_F. (e) Extracted Eliashberg function. (f) EPC strength estimated from the Eliahsberg function and plotted as a function of T_c.

d-electron-phonon coupling near 12 meV. In contrast, ReΣ(ω) of the α band only shows a broad shoulder. Through a fit to the extracted ReΣ(ω) following the maximum energy method [3], we extract the Eliashberg function, $\alpha^2F(\omega)$. The extracted $\alpha^2F(\omega)$ for the α and β bands are plotted in Fig. 1f. The orbital dependence of the EPC is mirrored in the different shapes of $\alpha^2F(\omega)$, where phonon modes near 32 meV are accounted for 70% of the total EPC strength on the α band, λ_p, but less than 50% for the EPC strength on the β band, λ_d. Interestingly, due to the spectral weight redistribution in $\alpha^2F(\omega)$ [shaded area in Fig. 1f], λ_p and λ_d calculated by $2\int_0^{\omega_{max}}\left[\frac{\alpha^2F(\omega)}{\omega}\right]d\omega$ are similar with $\lambda_{p,d} \sim 0.45 \pm 0.05$. Theoretically, λ can approximately be derived from a simpler approach following $\lambda_{dev} = \partial \mathrm{Re}\Sigma(\omega)/\partial\omega|_{\omega = E_F} \cong \lambda$, when *T* is far lower than the Debye temperature. At $T = 6$ K, this method yields $\lambda_{dev} \sim 0.6 \pm 0.1$. By scanning the kinks along with the FSs, the extracted $\lambda_{dev}(\boldsymbol{k})$ for the α and β bands of two independent samples are summarized in Fig. 1g, which shows a nearly isotropic behavior within experimental uncertainties.

The orbital- and momentum-dependent results demonstrate that λ in CsV_3Sb_5 falls in the intermediate range of 0.45 – 0.6, which is about 2 times larger than the previous DFT predicted $\lambda_{DFT} \sim 0.25$ [1]. Using McMillan's formula and taking the lower and upper limits of the experimentally estimated λ and the logarithmic mean phonon frequency ~17.1 meV obtained by $2/\lambda\int_0^{\infty} ln\omega\left[\frac{\alpha^2F(\omega)}{\omega}\right]d\omega$, we derive T_c in a range from 0.8 K to 3 K. The upper limit is comparable to the experimentally determined T_c in CsV_3Sb_5 (Fig. 2a).

As T_c of CsV_3Sb_5 can be increased with chemical substitutions or external pressure (Fig. 1a). We thus continue to examine the EPC strength in 7% Nb-doped $Cs(V_{0.93}Nb_{0.07})_3Sb_5$ with $T_c \sim 4.4$ K. Electronic kinks are observed on both the α and β bands as shown in Fig. 2b for the ARPES intensity plots and Fig. 2c for the extracted band dispersions. Figure 2d shows the extracted ReΣ(ω) on the α and β bands of $Cs(V_{0.93}Nb_{0.07})_3Sb_5$. Remarkably, we observe that while ReΣ(ω) on the α band is similar in $Cs(V_{0.93}Nb_{0.07})_3Sb_5$ and CsV_3Sb_5, on the β band, it shows a strong enhancement in the Nb-doped sample, especially near $E_B \sim 10$ meV. Based on the extracted $\alpha^2F(\omega)$, shown in

Fig. 2e, we find that $\lambda_d \sim 0.75 \pm 0.05$ is enhanced by about 50% in $Cs(V_{0.93}Nb_{0.07})_3Sb_5$ (Fig. 2f). Importantly, the enhanced λ_d is expected to elevate T_c up to 4.5 K, which is comparable to the experimental value of 4.4 K. Such synchronous enhancements of λ_d and T_c may indicate that the V 3*d*-electron–phonon couplings are the main driver of the superconductivity in CsV_3Sb_5.

In summary, by investigating the electronic kinks, we determined the intermediate EPC that is twice larger than the DFT calculation in the kagome superconductors CsV_3Sb_5 and $Cs(V_{0.93}Nb_{0.07})_3Sb_5$. Our results provide an important clue to understand the pairing mechanism in CsV_3Sb_5. The orbital and momentum dependence of the electronic kinks and their strengthening with the promoted T_c prove that the EPC in CsV_3Sb_5 is strong enough to support T_c comparable to the experiment value and hence cannot be excluded as a possible pairing mechanism.

References

[1] H. Tan *et al.*, Phys. Rev. Lett. **127**, 046401 (2021).
[2] B. Ortiz *et al.*, Phys. Rev. Lett. **125**, 247002 (2020).
[3] Y. Zhong *et al.*, Nat. Commun. **14**, 1945 (2023).

Authors

Y. Zhong, S. Li[a], H. Liu[b], Y. Dong, K. Aido, Y. Arai, H. Li[a], W. Zhang[c], Y. Shi[b], Z. Wang[d], S. Shin, H. N. Lee[a], H. Miao[a], T. Kondo, and K. Okazaki
[a]Oak Ridge National Laboratory
[b]Chinese Academy of Sciences
[c]Sophia University
[d]Boston College